RESEARCH ARTICLE

The hydrogen puzzle in rock-enhanced biochar: Pyrogenic coating, mineral redox and pore accessibility

Johannes Meyer zu Drewer[1,2,3]*, Tobias Bromm[4], Thomas D. Bucheli[2], Pellegrino Conte[5], José María de la Rosa[6], Harald Fitzek[7,8], Amin Ghafarpour[9], Bruno Glaser[4], Andreas Kappler[10,11,12], Calogero Librici[5], Jens Möllmer[13], Michael Oberaigner[7,8], Sara Maria Pérez-Dalí[6], Arka Rudra[14], Águeda Sánchez-Martín[6], Hamed Sanei[14], Hans-Peter Schmidt[15], Nikolas Hagemann[1,2,15]*

1 Ithaka Institute, Goldbach, Germany, **2** Environmental Analytics, Agroscope, Zürich, Switzerland, **3** Institute of Sustainable Energy Systems, Offenburg University, Offenburg, Germany, **4** Institute of Agricultural and Nutritional Sciences, Martin Luther University Halle-Wittenberg, Halle, Germany, **5** Department of Agricultural, Food and Forest Sciences, University of Palermo, Palermo, Italy, **6** Instituto de Recursos Naturales y Agrobiología de Sevilla, IRNAS-CSIC, Seville, Spain, **7** Graz Centre for Electron Microscopy (ZFE), Graz, Austria, **8** Institute of Electron Microscopy and Nanoanalysis (FELMI), Graz University of Technology, Graz, Austria, **9** Terrestrial Paleoclimatology and Paleontology, Eberhard Karls University Tübingen, Tübingen, Germany, **10** Geomicrobiology, Department of Geosciences, University of Tuebingen, Tuebingen, Germany, **11** Cluster of Excellence: EXC 3121: TERRA – Terrestrial Geo-Biosphere Interactions in a Changing World, University of Tübingen, Germany, **12** Cluster of Excellence EXC 2124, Controlling Microbes to Fight Infection, University of Tuebingen, Tuebingen, Germany, **13** Institute for Non-Classical Chemistry e.V. (INC), Leipzig, Germany, **14** Lithospheric Organic Carbon Group, Department of Geoscience, Aarhus University, Aarhus, Denmark, **15** Ithaka Institute, Arbaz, Switzerland

* Nikolas.hagemann@agroscope.admin.ch, mzd@ithaka-institut.org

Check for updates

OPEN ACCESS

Citation: Meyer zu Drewer J, Bromm T, Bucheli TD, Conte P, María de la Rosa J, Fitzek H, et al. (2026) The hydrogen puzzle in rock-enhanced biochar: Pyrogenic coating, mineral redox and pore accessibility. PLoS One 21(8): e0355781. https://doi.org/10.1371/journal.pone.0355781

Editor: Karthik Kannan, National Chung Cheng University College of Engineering, TAIWAN

Received: March 5, 2026

Accepted: July 24, 2026

Published: August 12, 2026

Copyright: © 2026 Meyer zu Drewer et al. This is an open access article distributed under the terms of the Creative Commons Attribution License, which permits unrestricted use, distribution, and reproduction in any medium, provided the original author and source are credited.

Data availability statement: All relevant data are within the paper and its Supporting Information files.

Funding: This research project was funded by the Deutsche Forschungsgemeinschaft (DFG, German Research Foundation) – 467391808.

Abstract

Rock-enhanced (RE-)biochars, produced by co-pyrolysis of silicate rock powder with biomass, were proposed to combine pyrogenic carbon capture and storage (PyCCS) with enhanced rock weathering (ERW) as complementary carbon dioxide removal approaches. Catalytic effects of rock-derived AAEM on pyrolysis and carbon speciation were anticipated. Here we produced six RE-biochars (10–90% rock content) by co-pyrolysis of basanite rock powder with wood at contrasting highest treatment temperatures of 450 °C and 750 °C. To provide an in-depth physico-chemical characterization of the RE-biochars, focusing on the biochar-mineral interface region, analytical methods including random reflectance, fast field cycling proton nuclear magnetic resonance relaxometry and electron energy loss spectroscopy were employed. While most treatments had limited effect on the biochar carbon yield (y_c) and aromaticity of the pyrogenic carbon, RE-biochar produced at 750 °C and containing 90% rock showed an increased hydrogen to carbon molar ratio ($H:C_{org}$), which we partly explained by i) contribution of geogenic hydrogen, ii) physical adsorption of hydrogen to minerals and iii) pyrogenic coating of rock particles with secondary char containing aliphatic- and carboxylic moieties. Still, we cannot fully identify the reasons for increased hydrogen content with constant aromaticity. A decreased reflectance (Ro) and thermal stability

AK acknowledges infrastructural support by the DFG under Germany's Excellence Strategy, Clusters of Excellence EXC2124 and EXC 3121. The thermo-gravimetric analyses (TGA) were funded by RES2SOIL project (PID2021-126349OB-C22) by the Ministerio de Ciencia e Innovación (MCIN/AEI/10.13039/501100011033). The funders had no role in study design, data collection and analysis, decision to publish, or preparation of the manuscript.

Competing interests: Hans-Peter Schmidt reports a relationship with Carbon Standards AG that includes board membership. Hans-Peter Schmidt and Nikolas Hagemann are authors of the Carbon Standards AG guidelines for the certification of biochar quality assurance (EBC) and biochar-based carbon sinks (EBC C-Sink/Global Biochar C-Sink, Global Artisan C-Sink). Hamed Sanei is a co-founder of Fusinite Ltd. These interests are fully disclosed in the manuscript. This does not alter our adherence to PLOS ONE policies on sharing data and materials.

(BC_{1000C}) for RE-biochars with 90% rock content, despite similar aromaticity as quantified by hydropyrolysis, highlight the limitations of analytical methods developed for carbonaceous materials in the assessment of high ash biochars. Co-pyrolysis can reduce metal oxides, such as hematite (Fe-III) to magnetite, producing (potentially) reactive metals species and can accumulate geogenic potassium (K) at micron scale at rock particle surfaces. This study provides evidence that co-pyrolysis of biomass and basanite does not increase y_c but alters the mineral speciation and elemental distribution at the surface of rock particles. These findings may be further exploited in the design of functionalized RE-biochars and in ERW research.

1. Introduction

The co-pyrolysis of biomass with exogeneous minerals was suggested to design functional biochars [1,2]. The presence of mineral matter in biomass pyrolysis impacts the relative yields of gaseous, liquid, and solid pyrolysis products as well as their carbon speciation. Those effects were shown for minerals inherently present in biomass [3] and for additives like salts, or wood ash [4–6]. The deliberate addition of mineral matter to the feedstock before pyrolysis is referred to as co-pyrolysis. Potassium salts can, e.g., improve phosphorus availability in sewage sludge char by the formation of soluble potassium hydrogen phosphate during pyrolysis [7]. Silica, iron salts and other metals were applied to improve the capacity of biochar to sorb organic micropollutants [8]. Underlying mechanisms may include alterations to biochar carbon speciation and porosity, but also the formation of specific mineral surfaces during pyrolysis, e.g., the reductive formation of magnetite, a mixed valence iron mineral from the Fe(III) mineral siderite [9] or the formation of Fe(0) from Fe(III)-hydroxide [10].

Mineral additives can also increase the biochar carbon yield (y_c), i.e., the fraction of biomass carbon converted to solid state pyrogenic carbon (PyC) during (co-)pyrolysis [11–13]. This was demonstrated for biomass co-pyrolyzed with wood-ash [6] or potassium acetate [5]. Improved mass conversion is mediated by catalytic effects [12], the formation of organo-metallic bonds [14], or the (partial) encapsulation of biomass [8,15]. Alkali and alkaline earth metals (AAEM) contained in mineral additives appear to be most relevant for the catalytic reduction of activation energy for biomass decomposition and the promotion of C–C cross-linkage formation, which together increases secondary char formation [6,16].

Silicate rock powder, as employed for enhanced rock weathering (ERW) [17–19] and for soil remineralization [20–22], was suggested as an abundant mineral additive to produce rock-enhanced (RE-)biochar [23–25]. Meyer zu Drewer *et al.* [24] showed that rock powder particles received a pyrogenic coating during co-pyrolysis, i.e., secondary char condensates on their surfaces, which could enhance y_c by increasing secondary char formation. However, y_c and aromaticity remained unaltered despite rock powder addition. Alkali and alkaline earth metals, when embedded in a (crystalline) silicate rock matrix, seem to remain, opposite to the above, largely unexposed

and non-reactive at highest treatment temperatures (HTT) of 650 °C. Since rock powder has a significantly higher thermal conductivity than biomass, it has been suggested that this leads to a higher pyrolysis intensity (i.e., higher heating rate and thus in longer exposure to the HTT) within biomass-rock powder pellets compared to pure biomass [22].

In the present study, we investigate how co-pyrolysis is altering the physico-chemical properties of RE-biochar, compared to pure biochar. We expand previous characterisations of RE-biochars [24,25] with a novel set of samples and a focus on microsites at the biochar-mineral interface, where a distinct PyC and mineral speciation may form during pyrolysis. Therefore, we produced six RE-biochars by co-pyrolysis of softwood with basanite rock powder at 450 °C and 750 °C. The RE-biochars contained 10 wt% (9:1), 50 wt% (1:1), or 90 wt% (1:9) basanite rock powder alongside two pure softwood biochars (BC450, BC750). Using random reflectance (Ro), hydropyrolysis (HyPy), benzene polycarboxylic acids (BPCA) molecular marker method, fast field cycling relaxometry proton nuclear magnetic resonance spectroscopy (FFC ^{1}H-NMR) and scanning transmission electron microscopy coupled to electron energy loss spectroscopy (STEM-EELS) and other analytical methods, we characterized the PyC speciation and discussed potential mechanisms affecting the latter. Both weathering and alkalinity production as well as the effect on plant growth of the (RE-)biochars characterized here, were investigated in Meyer zu Drewer et al. 2026 [26].

2. Results and discussion

2.1. Increased H:C_{org} ratio despite similar aromaticity: Where does the hydrogen come from?

Biochars were produced from pelleted, low-ash wood shavings (biomass composition S1 Table) at 450 °C and 750 °C in a continuously operated auger reactor [27]. These showed well-expected properties, mass yield (y_m), and y_c as shown in Table 1 [28–30]. Based on the y_m of the pure biochars, we mixed basanite rock powder (elemental and mineral composition, S2 Table) to the wood shavings prior to pelleting and pyrolysis to achieve the desired rock powder content in the RE-biochar.

Rock addition increased the ash content of the biochar in agreement with the rock amendment rate. Dry and ash-free (daf) organic carbon (C_{org}) content and y_c remained largely constant for RE-biochars produced at the same HTT (Table 1). The most remarkable effect of rock addition was the extremely high H:C_{org} molar ratio of 0.87 observed for the RE-biochar produced at 750 °C with 90% rock content (BC750–1:9). As pure basanite showed 0.3% hydrogen content in elemental analysis (0% C), we used this data to calculate a H:C_{org} molar ratio of the biogenic fraction, which was still considerably higher than expected (H_{bio}:C_{org} = 0.54). This calculation assumes that the rock, or at least its H content, remained unchanged by co-pyrolysis, which we examine in more detail below.

Lower dosages of rock powder had a limited effect on this biochar property and rather decreased the H:C_{org} molar ratio at 750 °C. At 450 °C, H:C_{org} molar ratio increased only slightly with increasing rock content. To verify these results, we reproduced all samples (S3 Table) with the difference that pelleting was not carried out in the lab but by a service provider and thus presumably under different pressure conditions (higher pellet density in 2nd batch). In this 2nd batch, the BC750–1:9 sample had a H:C_{org} molar ratio of 0.67 (H_{bio}:C_{org} = 0.37) (S4 Table), which is lower than in the first experiments but still much higher than the control and generally higher than expected for a biochar made at this HTT. Such high H:C_{org} molar ratios are almost unprecedented at a HTT of 750 °C [29,30]. Yang et al. [13] have documented an increase of H:Corg molar ratios in biochar produced at 500 °C from 0.2-0.3 to 0.3-1.3 for the addition of various minerals and salts, including $Ca(H_2PO_4)_2$, which caused the maximum values.

Still, a quantification of BPCA markers (%BPCA-6) [31] and hydropyrolysis (HyPy) [32,33] did not reveal any considerable changes due to rock enhancement, which strongly suggests that changes in H:C_{org} ratio (Table 1) are not the result of changes in biochar's aromaticity. For HTT 450 °C, BPCA-6 – the hexacarboxylated benzene marker indicative of highly condensed aromatic domains in biochar, accounted for 23.3%−27.6% of total BCPAs and 42.7%−58.4% of C_{org} resisted HyPy (BC_{HyPy}), representing the aromatic carbon moieties of eight or more condensed rings. For HTT 750 °C, BPCA-6 presented 69.6%−73.4% of total BCPAs and BC_{HyPy} 95.6%−97.4% of C_{org}. Also, absorption spectra obtained by

Table 1. Basic physico-chemical properties of biochar and rock-enhanced biochar (BC) produced at 450 °C (450) or 750 °C (750), containing 0 (-), 10% (9:1), 50% (1:1) or 90% (1:9) basanite rock powder. Data on main- and trace element content are presented in S7 Table and basic properties of basanite in S2 Table).

	BC450	BC450–9:1	BC450–1:1	BC450–1:9	BC750	BC750–9:1	BC750–1:1	BC750–1:9
Mass yield (y_m in%)[1]	25.6 ± 0.5	28.0 ± 0.3	40.5 ± 1.2	72.7	18.9 ± 0.7	24.7 ± 0.1	33.4 ± 0.2	66.4
Carbon yield (y_c in %)[1]	42.9 ± 0.9	43.7 ± 0.4	40.3 ± 1.2	46.6	35.2 ± 1.2	41.3 ± 0.2	35.5 ± 0.2	38.3
Rock content (%)	0	5.7	50.2	89.1	0	8.3	49.9	89.1
Biogenic content (%)	100	94.3	49.8	10.9	100	91.7	50.1	10.9
Total ash (%)	1.9	7.5	51.2	89.3	3.0	11.0	51.3	89.4
Biogenic ash (%)	1.9	1.8	1.0	0.2	3.0	2.7	1.4	0.3
Carbon (C, %)	85.0	76.7	41.5	9.3	94.3	83.6	46.2	9.7
Organic C (C_{org},%)	84.8	76.7	41.5	9.3	93.9	83.2	45.8	9.6
$C_{org\ daf}$ (% of C_{org})	86.4	87.1	86.1	86.1	96.5	95.0	96.0	98.0
$C_{vol.HAWK}$ (mg g^{-1} C_{org})[2]	10.9	11.7	10.7	12.9	0.3	0.4	0.7	3.3
BC_{HyPy} (% of C_{org})[3]	56.4	58.4	49.5	42.7	97.3	95.6	97.4	97.2
TIC (%)[4]	0.2	< 0.1	< 0.1	< 0.1	0.4	0.4	0.4	0.1
Hydrogen (H, %)	3	2.9	1.7	0.4	1.3	0.8	0.5	0.7
Nitrogen (%)	0.29	0.06	< 0.05	< 0.05	0.33	0.41	0.15	< 0.05
Sulfur (%)	< 0.03	< 0.03	< 0.03	< 0.03	< 0.03	< 0.03	< 0.03	< 0.03
Oxygen (%)	9.8	8.4	5	1.2	1.3	2.8	0.9	<LOQ
H:C_{org} molar ratio	0.42	0.45	0.49	0.51	0.16	0.11	0.13	0.87
H_{Bio}:C_{org} molar ratio[5]	0.42	0.45	0.44	0.17	0.16	0.11	0.09	0.54
SEC (µS cm^{-1})[6]	$6.0x10^{-5}$	$4.7 x10^{-5}$	$1.6 x10^{-5}$	$<9.6x10^{-7}$	$1.3 x10^{3}$	$1.7 x10^{3}$	$7.6 x10^{2}$	$4.5 x10^{1}$
SSA (m^2 g^{-1})[7]	1.4	4.3	3.3	9.1	447	421	231	23
***∑BPCA-3 (%)*[8]**	7.6	7.8	8.5	8.0	0.9	0.8	1.0	1.4
∑BPCA-4 (%)	26.5	27.3	27.0	28.4	6.4	6.0	6.0	7.8
∑BPCA-5 (%)	38.3	39.5	37.5	40.2	21.7	19.8	30.8	21.2
∑BPCA-6 (%)	27.6	25.4	27.1	23.2	71.0	73.4	72.2	69.6
∑BPCA 3−6 (g C kg^{-1})	106.1	86.7	47.3	13.8	125.6	111.1	74.9	13.7

[1]Variability *calculated as mean x coefficient of variation (CV%) of biochar transport-rate (t_b; n = 3), not available for BC450–1:9 and BC750–1:9.*

[2]*Fraction of carbon being volatilized between 300–650 °C during analytical pyrolysis on a HAWK-pyrolizer.*

[3]Fraction of organic carbon resistant to hydropyrolysis.

[4]Total inorganic carbon.

[5]*H:C_{org} molar ratio of the biogenic fraction, i.e., bulk H:C_{org} corrected for geogenic hydrogen and carbon in the sample (Equation 6).*

[6]*Solid state electric conductivity. Limit of detection is sample specific, calculated from biochar pellets height after compression at 160 MPa (BC450–1:9 = 4.5 mm distance between anode and cathode) and maximum resistivity measurable with the Black Gauss I (*100 x 10^6 Ohm). *LOQ = Limit of quantification. SEC = solid-state electrical conductivity.*

[7]Specific surface area quantified by nitrogen gas adsorption and quantified using BET-method.

[8]*BPCA = Benzenepolycarboxylic acid marker as detailed in the Methods.*

https://doi.org/10.1371/journal.pone.0355781.t001

Fourier-transformed infrared spectroscopy (FTIR) and Raman spectroscopy revealed no difference in bulk carbon speciation between (RE-)biochars produced at the same HTT. Fourier transformed infrared spectroscopy showed the presence of aromatic C = C bonds at 1589 cm^{-1} and absence of symmetric- and asymmetric aliphatic carbon structures (2840-2890 cm^{-1} and 2920−2990 cm^{-1}, respectively) in all samples (S5 Fig). Raman spectroscopy revealed that ratios of D/G intensity- and area ratios were indifferent between samples obtained at the same HTT (S6 Fig). The G band at 1600 cm^{-1} relates to C-C linkages in aromatic moieties, i.e., the degree of graphitization. The D band at 1345 cm^{-1} relates to structural defects of the latter [34]. As the aromatic backbone remained largely unchanged compared to the control biochar, the increase in

the H:C_{org} molar ratio can only be explained by an increase of the H content of the mineral phase and/or an increase of the H:C_{org} molar ratio in the non-BC_{HyPy} fraction. This may result from aliphatic compounds (e.g., alkanes, H:C ≈ 2) in the pyrogenic coating of the rock surface [24]. This aliphatic- or small aromatic systems would be included in measured non-BC_{HyPy} fraction or the S1&S2 fraction of sequential HAWK pyrolysis (c.f. section 2.1.1).

2.1.1. Hydrogen bound in semi-volatile organic compounds. An increase in non-BC_{HyPy} should correspond to a decrease in thermal stability and an increase in thermally labile, i.e., volatile organic compounds. We quantified the daf mass loss ($m_{vol,TGA}$) of 5 mg (RE-)biochar in the range of 50−1000 °C at 10 °C min^{-1} thermo-gravimetric analysis (TGA). In parallel, a HAWK-pyrolizer with coupled C_{org}-analyzer quantified carbon loss ($C_{vol,HAWK}$) from 10 mg sample in the range of 300−650 °C at 25 °C min^{-1} [35]. Both analyses ran under inert atmosphere. The content of $C_{vol,HAWK}$ (Table 1) increased with rock powder content from 10.9 and 0.3 mg $C_{vol,HAWK}$ per gC_{org} at 0% rock to 12.9 and 3.3 mg $C_{vol,HAWK}$ per $g^{-}C_{org}$ for biochars containing 90% rock that were produced at HTT of 450 °C and 750 °C, respectively. The increase was small at 10% and 50% rock but pronounced at 90% rock content. Likewise, $m_{vol,TGA50-350°C}$ was 2−4% of daf biochar for samples with 0−50% rock content but 9% from BC450–1:9 and 21% from BC750–1:9 (Fig 1). The same trend is observed for $m_{vol,TGA350-650°C}$ (corresponding to the HTT of the HAWK pyrolizer), except for BC450. Still, the $C_{vol,HAWK}$ fraction of daf biochar is < 1% and cannot solely explain the reduced thermal stability observed in equivalent temperature ranges. The fraction of daf biochar ultimately resisting to thermal degradation at the end of the TGA temperature ramp is referred to as BC_{1000C} (%). The strongly increased BC_{1000C} fraction in RE-biochars produced at HTT 450 °C, same as the complete loss of BC_{1000C} from the BC750–1:9 sample cannot rationally be explained by their initial PyC speciation (Fig 1). We elucidate potential limitations of methods, which were initially developed for carbonaceous materials, in the thermal analysis of RE-biochars in section 2.5.

The solid-state electrical conductivity (SEC) of RE-biochar decreased compared to pure biochar, which was expected because silicate rock is an electric insulator. However, SEC was higher than in the equivalent post-pyrolysis mixtures (PPMs) of pure biochar and rock powder (Fig 1C + D). These results are consistent with Meyer zu Drewer *et al.* [24], who co-pyrolyzed the same basanite with landscaping wood on the same pyrolysis unit at 650 °C. They attributed the increased SEC to pyrogenic coatings of rock particles with conductive, soot-like secondary char formed from gaseous pyrolysis products [36,37]. Such secondary char contains condensed aromatic structures and condensates of tar [38]. Condensates are typically more hydrogenated than a primary aromatic lattice [39], which may partially explain the elevated H:C_{org} molar ratio of RE-biochars. Sorption of volatile organic carbon onto SiO_2-rich mineral surfaces [40] can provide nucleation sites for secondary char. Both in Meyer zu Drewer *et al.* [24] and in the present study, rock enhancement did not change y_c. Thus, the amount of carbon from secondary char coating is quantitatively minor compared to the total carbon yield. It can be concluded that small, hydrogenated carbon species, as approximated by $C_{vol.HAWK}$ content (dummy H:C_{org} ratio = 2; aliphatic carbon) and non-BC_{HyPy} content (dummy H:C_{org} ratio = 0.625; pyrene) contribute only to a negligible extend to the total H content of the biochar (S8 Table).

2.1.2. Hydrogen associating or reacting with minerals. Gaseous hydrogen (H_2) is an inherent by-product of biomass pyrolysis [41–43]. Its production increases with HTT and may exceed 50 vol% of the pyrolysis gas depending on feedstock selection and process conditions [44,45]. Physi- and chemisorption of H_2 to silicate minerals can occur in consequence of a solid-gas exchange where H_2 or other H-bearing volatiles are present. The sorption of H_2 to minerals is dominated by physical adsorption [46]. Silicate minerals can be polar due to isomorphic substitution, charged surfaces and edges or functional groups such as silane groups (Si-OH). Hydrogen can easily be polarized and bind to charged mineral surfaces by van der Waals forces [47]. The adsorption capacity increases with micro porosity and specific surface area (SSA) [46]. Consequently, H_2 sorption to dense minerals such as pyroxene or plagioclase is likely limited but considerable for amorphous Fe-oxides and layered silicates. Especially defect sites and the interlayer space (>2.9 Å) in 2:1-layer silicates are relevant for H_2 adsorption [43–45,48]. Catalytic metals can further enable hydrogen spillover to surfaces that otherwise do not bind H under identical conditions [49].

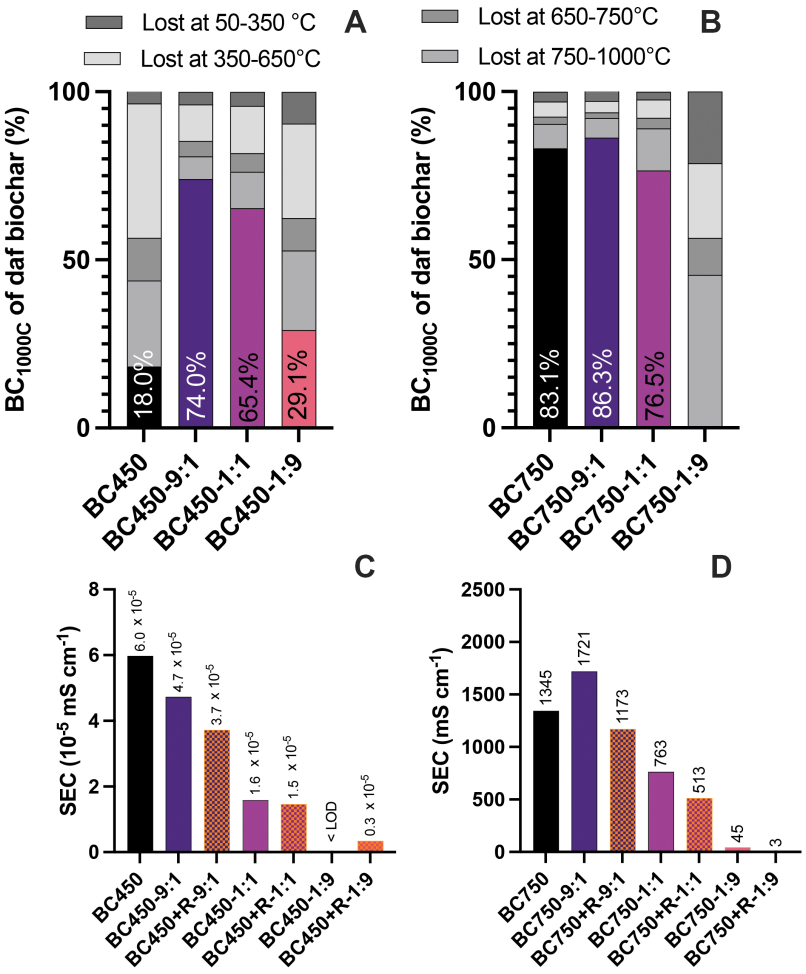

Fig 1. Top: Thermogravimetric analysis of rock-enhanced biochars: Mass loss (%) of dry and ash free (daf) biochar in specific temperature ranges (in gray scale) and fraction retained at 1000 °C (BC_{1000C}). Bottom: *Solid-state electrical conductivity (SEC) in mS cm*$^{-1}$. (A + C): *Rock-enhanced biochars pyrolyzed at 450 °C (BC450) containing 10-90% basanite (BC450-9:1, BC450-1:1 and BC450-1:9),* (B + D): *Rock-enhanced biochars pyrolyzed at 750 °C (BC750), containing 10-90% basanite (BC750-9:1, BC750-1:1 and BC750-1:9). Orange shaded bars with BC + R notation denote equivalent post pyrolysis mixtures of biochar and rock powder. LOD = Sample specific limit of detection, calculated from biochar pellets height after compression at 160 MPa (4.5-6.0 mm = distance between anode and cathode) and maximum resistivity measurable with the setup (*100 x 10^6 Ohm).

https://doi.org/10.1371/journal.pone.0355781.g001

Lastly, H (respectively H_2O) can also be structurally incorporated in nominally anhydrous minerals and isomorphically substitute geogenic metal ions such as Mg^{2+}. This was demonstrated for olivine under extremely high pressure and temperature regimes. At 1 atm, this process is much more limited and likely restricted to surface sites. Natural, nominally anhydrous olivine contains < 0.05 mol H kg^{-1} [50,51]. Sundvall & Skogby (2011) [52] investigated the protonation of pyroxene under varying conditions. Under 1 atm up to 700 °C they found that most pyroxenes lost H while hydration was only observed for pyroxenes rich in iron (Fe). They explained this observation by a surface redox reaction. Olivine and pyroxene are both present in the basanite employed here, which also contains 7.8% Fe (S2 Table).

We used X-ray diffraction (XRD) to detect possible changes in the mineralogy of basanite thermally treated in the absence of biomass and basanite co-pyrolyzed to form RE-biochars (9:1). The heating of pure rock powder had no effect on the speciation of silicate minerals (R450 and R750 in S2 Table). The content of all silicate minerals in the 450 °C RE-biochars was in good agreement with expected, calculated concentrations. In RE-biochars produced at 750 °C, the

content of all silicate minerals fell below the expected values, while the amorphous fraction increased (Table 2); for example, the detected content of the potassium (K)-bearing mineral leucite was 50% below the expected value. We assume that X-ray diffraction was not affected by the presence of PyC as illustrated by the successful detection of calcite in pure BC750, despite a total inorganic carbon (TIC) content of < 1%. In summary, the assessment of bulk mineralogy confirmed changes induced by co-pyrolysis that were absent in thermal treatment without biomass, but did not directly prove H uptake. Further research should employ X-ray photoelectron spectroscopy (XPS) to investigate changes in binding energy in surface minerals only.

The inorganic phase is generally a more relevant contributor to elevated $H:C_{org}$ ratios than low molecular weight hydrocarbons. The contribution of geogenic hydrogen can explain 50% of the increase in $H:C_{org}$ observed in BC750–1:9 compared to BC750 ($H:C_{org}$ *versus* $H_{Bio}:C_{org}$). The sorption of a dense monolayer of H_2 to the rock surfaces (BET-surface, section 4.2) present in BC750–1:9 could explain about 5% of the remaining delta between the $H_{Bio}:C_{org}$ of BC750 and BC750–1:9. However, this can be both an over- and underestimation. On the one hand, not all mineral surfaces are exposed (pyrogenic coating) and not all sorb H_2 well. On the other hand, small interlayer spaces of phyllosilicates (0.3-0.4 nm; most relevant for H_2 sorption) are not accounted for in BET analysis. Hydrogen can enter pores inaccessible for N_2. We acknowledge that there must be additional, unknown drivers contributing to elevated $H_{Bio}:C_{org}$ which were not quantified here. One possible scenario is the "*lock-in*" of water that may have formed as a product of redox reactions or in the syngas. Water may be structurally integrated in minerals (hydration) or retained in obstructed parts of the biochar pore system (section 2.3)

Table 2. Concentration of mineral species in pristine basanite rock powder (R), pure biochar (BC450, BC750) and selected rock-enhanced (RE-) biochars produced at 450 °C containing 10% rock (RE-BC450-9:1) and produced at 750 °C containing 10% rock (RE-BC750-9:1) based on X-ray diffraction (XRD) measurements. The data is presented in mass-%.

Mineral Group	Mineral Formula	R	BC450	BC450–9:1		BC750	BC750–9:1	
				expected*	measured		expected*	measured
Quartz	SiO_2	0.5	<0.1	0	0.1	<0.1	0	<LOD
Plagioclase	$(Na,Ca)(Si,Al)_4O_8$	12.9		0.7	0.8		1.1	0.8
Clinopyroxene	$(Ca,Na)(Mg,Fe,Al,Ti)(Si,Al)_2O_6$	45.6		2.6	2.5		3.8	2.6
Olivine	$(Mg,Fe)_2SiO_4$	4.5		0.3	0.2		0.4	0.3
Nepheline	$(Na,K)AlSiO_4$	11.3		0.6	0.6		0.9	0.8
Sodalite	$Na_8Al_6Si_6O_{24}Cl_2$	0.4		0	<LOD		0.0	<LOD
Leucite	$KAlSi_2O_6$	12.6		0.7	0.7		1.0	0.5
Analcime	$NaAlSi_2O_6•(H_2O)$	0.8		0	<LOD		0.1	<LOD
Hauyne	$(Na,Ca)_{4-8}Al_6Si_6(O,S)_{24}(SO_4,Cl)_{1-2}$	0.3		0	<LOD		0	<LOD
2:1-layer silicates	$(K,H_3O)(Al,Mg,Fe)_2(Si,Al)_4O_{10}[(OH)_2,H_2O]$	2.7		0.2	<LOD		0.2	<LOD
Vesuvianite	$Ca_{10}Mg_2Al_4(SiO_4)_5(Si_2O_7)_2(OH)_4$	1.3		0.1	<LOD		0.1	<LOD
Pseudobrookite	$(Fe^{3+},Fe^{2+})_2(Ti,Fe^{2+})O_5$	0.2		0	<LOD		0	<LOD
Hematite	Fe_2O_3	5.8		0.3	0.1		0.5	<LOD
Ilmenite	$Fe^{2+}TiO_3$	0.3		0	<LOD		0	<LOD
Calcite	$CaCO_3$	0	0.2	0.2	0.1	0.9	0.8	0.1
Apatite	$Ca_5(PO_4)_3(OH,F,Cl)$	0.9		0.1	<LOD		0.1	<LOD
Amorphous		0	99.8	94.1	94.8	99.1	90.8	94.9

*Expected concentrations of mineral species in RE-biochars calculated based on XRD measurements of pure basanite, BC450, BC750 and the rock/biogenic fractions of the RE-biochars. LOD = Limit of detection.

https://doi.org/10.1371/journal.pone.0355781.t002

In summary, the elevated $H:C_{org}$ ratio in BC750–1:9 are attributed to multiple processes that differ in their degree of evidential support. First, the contribution of geogenic hydrogen is directly quantified from bulk elemental data and accounts for 50% of the observed increase relative to BC750. Second, physical adsorption of molecular hydrogen to mineral surfaces was estimated at 5% based on the BET SSA, which carries considerable uncertainties. Third, aliphatic and less condensed (lower-aromaticity) carbon species in secondary char have much higher $H:C_{org}$ molar ratio than the bulk biochar, though their minor mass fraction limits their quantitative contribution to the elevated $H:C_{org}$. Fourth, the retention of water formed during redox reactions or trapped in obstructed pore domains remains a speculative and hardly quantifiable mechanism, whose contribution is, however, considered marginal. Collectively, the processes identified so far do not fully account for the elevation in $H:C_{org}$, suggesting that additional mechanisms are at play.

2.2. Reduction of iron minerals during co-pyrolysis

The pyrolysis gas contains reducing agents such as H_2 or carbon monoxide, which could react with mineral components and are known to reduce iron at high temperatures [53–56]. X-ray diffraction showed that the content of the ferric iron mineral hematite (Fe_2O_3) fell below the limit of detection as the result of co-pyrolysis, in contrast to the thermal treatment of the rock powder without biomass (S2 Table). This can be explained by the reduction of Fe(III) to Fe(II), forming, e.g., magnetite or other reduced minerals such as siderite or vivianite. The disappearance of hematite is concomitant with an increase in magnetic susceptibility (χ), which quantitatively describes the content of ferrimagnetic compounds in a sample. It is determined by measuring the extent to which a sample of known volume and mass alters a magnetic field and is expressed in $m^3\ kg^{-1}$ [57]. Pure biochars contained only trace amounts of ferrimagnetic minerals ($3x10^{-8}\ m^3\ kg^{-1}$), whereas basanite rock powder showed more than 70 times higher levels ($2.25x10^{-6}\ m^3\ kg^{-1}$) that further increased to $2.77x10^{-6}\ m^3\ kg^{-1}$ upon thermal treatment at 750 °C. In RE-biochars, ferrimagnetic contents exceeded the expected mixture values, particularly at 750 °C (Fig 2). To the best of our knowledge, this is the first evidence that not only pure Fe minerals (e.g., hematite) can be reduced during the production of biochar [58], but also Fe minerals embedded in a silicate rock matrix.

2.3. ^{1}H FFC-Relaxometry: Effects on water–surface interactions and pore domain connectivity

Nitrogen sorption isotherms and the BET method showed that RE-biochars produced at 450 °C displayed higher surface areas than expected from the arithmetic combination of biochar and rock powder surface areas (S9A,B Fig). At 750 °C,

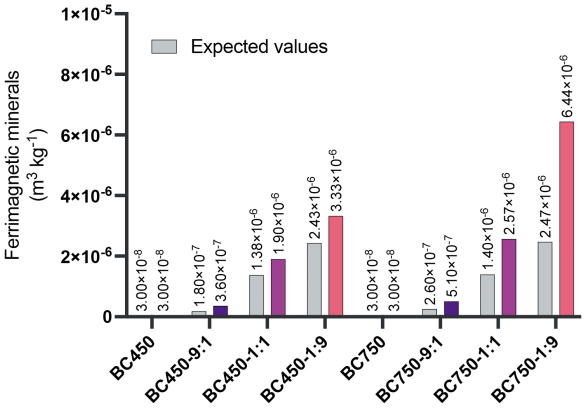

Fig 2. Measured content of bulk ferrimagnetic minerals in $m^3\ kg^{-1}$ sample and expected content of bulk ferrimagnetic minerals considering their respective biogenic and geogenic fraction and ferrimagnetic properties of the latter (grey). On the X-axis: Rock-enhanced biochars produced at 450 °C (BC450) containing 10−90 wt% basanite (BC450-9:1, BC450-1:1 and BC450-1:9) and rock-enhanced biochars produced at 750 °C (BC750), containing 10−90 wt% basanite (BC750-9:1, BC750-1:1 and BC750-1:9).

https://doi.org/10.1371/journal.pone.0355781.g002

surface areas decreased progressively with increasing rock content but remained within the expected range for mixtures containing up to 50% rock, whereas the 90% rock treatment showed a marked decline (56% below the expected value). This behavior likely reflects a substantial reduction in accessible pore domains due to obstruction of pores by minerals, as suggested by Meyer zu Drewer *et al.* [24]. To complement these structural measurements with a functional characterization of water-accessible domains, we employed fast field cycling (FFC) ^{1}H-NMR relaxometry. This technique probes the spin–lattice relaxation of water protons within porous matrices [59]. Relaxometry provides information on water–surface interactions, thereby allowing the assessment of pore-domain accessibility and connectivity in porous materials such as biochars.

The relaxation patterns in Fig 3 reveal three effects of co-pyrolysis with rock powder. First, the shift of T_1 distributions reflects HTT-dependent changes in the balance between water–surface and water–water relaxation. At 450 °C, rock addition shifts T_1 toward shorter values, indicating that water is more strongly bound to biochar and mineral surfaces. In contrast, at 750 °C, rock addition shifts T_1 toward longer values. This in turn is indicative for increasingly bulk-like relaxation environments where water interacts less strongly with biochar and mineral surfaces (i.e., more bi-polar water-water connections in larger pores). The observed opposite trends align with the HTT-dependent restructuring of accessible pore domains inferred from BET measurements, where the SSA increased with rock content at 450 °C but decreased at 750 °C. Second, the marked decrease in the pore connectivity index (PCI) indicates reduced exchange between relaxation domains, implying that water mobility becomes increasingly confined to domains that exchange less efficiently with each other. This observation implies a generally reduced mobility of liquids and potentially gases in RE-biochar. Third, in RE-biochars produced at 750 °C, the alteration of T_1 distributions is consistent with the formation

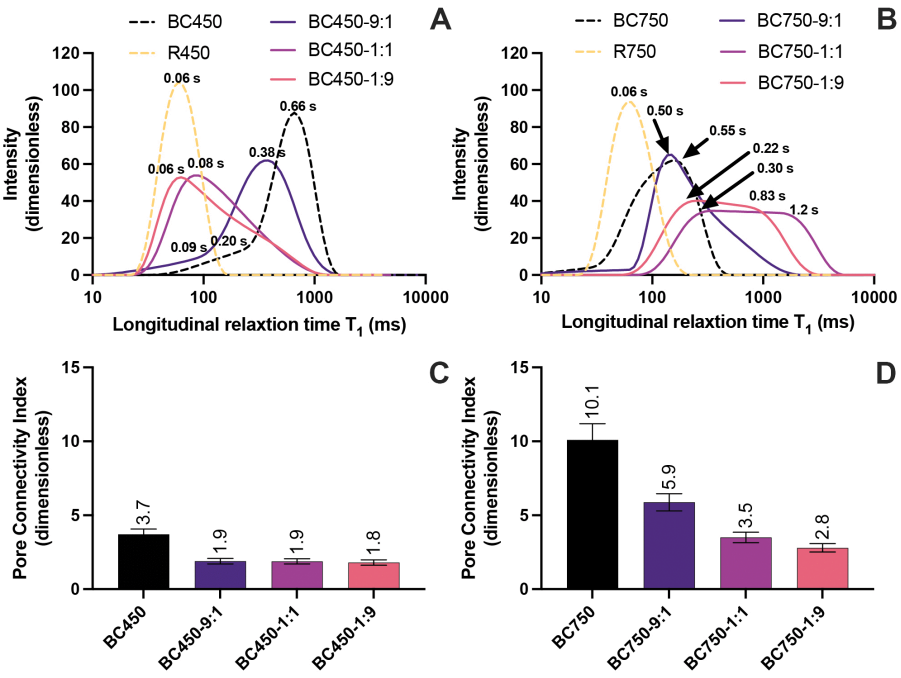

Fig 3. (A+B): Distribution histogram of measured longitudinal relaxation times (T_1) of hydrogen during fast field cycling nuclear magnetic resonance (FFC-NMR) relaxometry. Logarithmic scaled X-axis in milliseconds and in-figure labels in seconds. (C+D): Dimensionless pore connectivity index (PCI) based on T_1 relaxation times, presented as mean ± standard deviation. Left: (Rock-enhanced) biochars pyrolyzed at 450 °C (BC450) containing 10-90% basanite (BC450-9:1, BC450-1:1 and BC450_1:9). Right: (Rock-enhanced) biochars pyrolyzed at 750 °C (BC750), containing 10-90% basanite (BC750-9:1, BC750-1:1 and BC750-1:9). Measurements on pure basanite rock powder, after thermal treatment at 450 °C (R450) and 750 °C (R750) respectively are indicated as yellow dashed lines in panel A and B.

https://doi.org/10.1371/journal.pone.0355781.g003

of mixed-valence Fe(II)/Fe(III) oxides such as magnetite, generated through the reductive transformation of Fe-oxides during pyrolysis. Such paramagnetic phases can contribute to the overall relaxation behavior, and may locally increase relaxation efficiency (i.e., shorter T_1) Accordingly, the net shift toward longer T_1 at 750 °C is interpreted primarily as a pore-domain/ accessibility effect (more bulk-like water environments), with magnetic phases acting as an additional, superimposed contribution [57,60,61].

Altogether, these effects highlight a chemically active interfacial environment during the co-pyrolysis, leading to the restructuring of pore domains compared to pure biochar and mineralogical transformations that shape porosity and surface properties. Given these effects, it is plausible that, at sites enriched in reactive or partially reduced metals, a fraction of interfacial carbon may experience interactions stronger than those expected from simple physisorption, potentially including the formation of metal–carbon (M–C) linkages and complexes. Possible examples include carbides such as Fe_3C [62]. While such interactions could in principle contribute to the modified relaxation behavior, they cannot be detected by FFC-NMR alone and would require complementary high-resolution spectroscopic or microscopic analyses for verification. At this stage, M–C linkages can therefore be regarded as a possible, yet unconfirmed, additional contribution to the overall interfacial relaxation environment.

2.4. Carbon speciation at the biochar-mineral interface

Scanning transmission electron microscopy coupled to electron energy loss spectroscopy (STEM-EELS) was used to resolve elemental composition and carbon speciation in BC750–1:1 at the nanometer scale (Fig 4, S10 Fig). Six EELS transects crossing from biogenic components of RE-biochar into adjacent rock consistently showed the K edge of aromatic C at 284.9–285.5 eV [63] transitioning to the characteristic Si-O peak at 540 eV [64] within the mineral phase (Si-O peak cropped from Fig 4). These measurements revealed a distinct carbon speciation at the biochar-mineral interface. Aliphatic carbon features (σ(C–H) and σ(C–C) at 287–288 eV [65,66] were detected in 4 of 6 scans, while carboxylic features at 288.6 eV [63,67] occurred in 2 of 6 scans. Such aliphatic and oxygenated signals align with the known composition of volatile pyrolysis intermediates like furans, phenols, alkanes, alkenes or alkynes, and support the idea of a pyrogenic coating of mineral surfaces. Basanite is a non-acidic aluminosilicate rock, composed mainly of plagioclase, pyroxene, and nepheline. These minerals provide negligible Brønsted acidity and therefore behave similarly to other non-acidic silicate surfaces, which are known to sorb and stabilize radicals and oxygenated vapors rather than drive catalytic transformations [68,69]. Accordingly, the interfacial carbon detected here is most likely derived from adsorption and consistent with the thin pyrogenic coating [24]. The presence of organo-mineral bonds as suggested above could not be confirmed, but the limited number of STEM-EELS scans can neither refute their existence. The sorption of such low-molecular compounds with a high H content (e.g., H:C ≈ 2 in alkanes) – or more complex pyrogenic hydrocarbons is a minor contributor to elevated $H:C_{org}$ ratios.

Elevated concentrations of K were identified at the biochar-mineral interface in 3/6 scans (297–300 eV) [70] and a 2D EELS mapping revealed a *potassium shell* at the mineral surface (Fig 5). Beam-induced K migration [71] was excluded experimentally (Inversed beam trajectory; S10B Fig). Enrichment of biogenic ash around rock particles could in principle produce such a shell, but this would also result in proportional enrichment of other cations, which was not observed. Instead, pyrogenic free radicals [72,73] may mobilize K from the outer layers of K-rich basanite minerals such as nepheline or leucite, whose heterogeneous distribution at the micrometer scale – as confirmed by scanning electron microscopy coupled with energy dispersive X-ray spectroscopy (SEM-EDX, S11 Fig) – likely explains the occurrence of K enrichment in only 3 of 6 STEM transects. This process may lead to enhanced alkalinity production due to a stronger release of basic cations (such as K^+) in short-term weathering experiments using RE-biochar.

2.5. Matrix-effects of inorganic phases on biochar analysis

The inorganic constituents of RE-biochar differ fundamentally from aromatic carbon moieties. Where mineral enrichment is high (e.g., 90% rock), inorganic constituents contribute a relevant volume-fraction to the RE-biochar. In such a case,

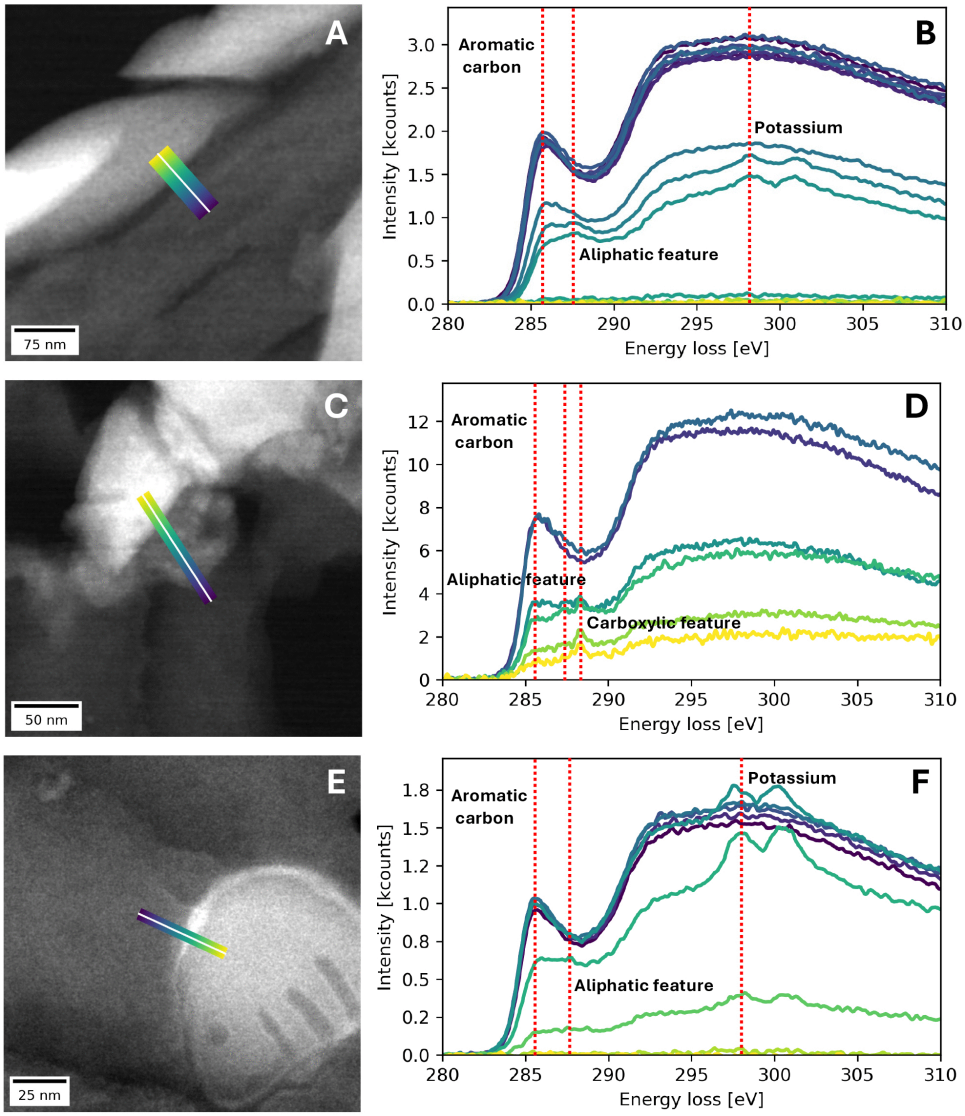

Fig 4. Left panels (A,C,E): Scanning transmission electron micrographs obtained in high-angle annular dark field mode (HAADF), showing ultrathin cross section of a BC750-1:1 pellet. Mineral particles (white) are embedded in the surrounding biochar matrix (dark) with an indicated measurement transect (color-coded) spanning the pure biochar (blue to purple) over the mineral-biochar interface (green to turquoise) into the rock particle (yellow to light green). Right panels (B,D,F): Corresponding electron energy loss spectroscopy (EELS) spectrograms obtained along the measurement transect. Note that the Si-O peaks are cropped from the spectra. Three additional spectrograms are shown in S10 Fig.

https://doi.org/10.1371/journal.pone.0355781.g004

interface regions are widely distributed and may become the spatially dominating surface in the system. Accordingly, it is necessary to critically examine whether established methods of biochar analysis can be applied to RE-biochar. It has been shown that the main and trace elements in RE biochar can be reliably quantified after chemical digestion, even though X-ray fluorescence is commonly used for rock [24]. The present study, however, revealed distortions in thermal and optical analytical techniques.

Following TGA (50−1000 °C), RE-biochars produced at 450 °C showed higher BC_{1000C} fractions than BC450, while BC_{1000C} for BC750–1:9 was zero. These findings cannot be reconciled with the results of HyPy and BCPA, which in

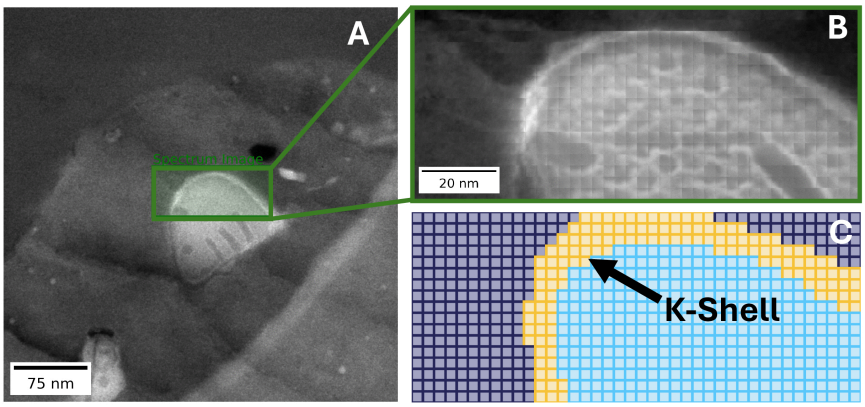

Fig 5. (A): Micrograph showing an ultrathin cross section of a BC750-1:1 pellet, with clipping (B) subjected to Electron Energy Loss Spectroscopy mapping of elemental distributions. (C): *Mapping of the distribution of the dominating elements: silicon-dominated rock particle (light-blue), carbon-dominated biochar matrix (dark-blue), potassium-rich shell (yellow).*

https://doi.org/10.1371/journal.pone.0355781.g005

turn provided a consistent picture. A likely source of error is the challenge to obtain a representative sample at the milligram-scale from a material with large density contrasts (biochar: ~ 0.2 kg L^{-1}; basanite: ~ 2.6 kg L^{-1}). If the actual ash content in the 5 mg subsample for TGA deviates strongly from the nominal value used for daf correction, mass loss and BC_{1000C} fraction may be over- or underestimated [24].

Matrix effects from the higher thermal conductivity and heat capacity of basanite compared to biomass and biochar may further distort apparent thermal stability [24]. Equivalent PPMs could not be reliably analyzed due to subsampling uncertainty at the milligram scale [24], and there was not enough biochar available for a mixture in the gram range followed by grinding in the vibratory ball mill. Therefore, the results of the thermal analysis of the RE-biochars can be unreliable and must be interpreted with caution. Demineralization of high-ash biochar samples, e.g., hydrofluoric acid treatment, is one option to be considered for the removal of silicates. It was shown that pre-analysis demineralization of samples can increase the predictive power of, e.g., elemental analysis and $H:C_{org}$ molar ratio to forecast actual aromaticity [74].

Random reflectance is increasingly used in biochar characterization [35,75–77]. For BC450, a mean Ro of 2.1% was recorded, which decreased to 1.7-1.9% in RE-biochars (Fig 6) and Ro% distributions were increasingly leptokurtic at 50−90% rock (narrowing of the curve = clustering of data around mean) with kurtosis of 1.7-3.0 (gaussian distribution = 3). This likely reflects a more homogeneous heating due to improved thermal conductivity of the rock–biomass mixture. For BC750 mean Ro was 4.3%, which increased to 4.5% in BC750–9:1 and BC750–1:1 and decreased to 3.6% in BC750–1:9 with increasingly platykurtic distribution (spreading of the distribution curve = larger standard deviation) with increasing rock content. Generally, HTT 450 °C samples were right skewed, i.e., the population had a lower median than mean, while HTT 750 °C samples were rather left skewed. These strong effects of rock-enhancement on Ro% distributions, despite nearly unchanged aromaticity (c.f. BC_{HyPy}, BPCA-6, FTIR, Raman) highlights that a high ash content can considerably impact Ro determination. It remains speculative whether this is due to the influence of the rock on the reflective properties or whether a proportion of the aromatic carbon now interacts with the rock in such a way that these structures can no longer be identified as macerals under a light microscope and thus not contribute to Ro. Therefore, Ro-derived metrics (e.g., persistence indices or carbonization temperatures) and mean Ro values of skewed distributions must be interpreted with caution. Both TGA and Ro highlight limitations of biochar analysis when applied to RE-biochars or high ash biochars in general. Future research but also routine analysis, such as for the European Biochar Certificate (EBC) [78], should explicitly account for these matrix effects in experimental design, sample preparation and data interpretation.

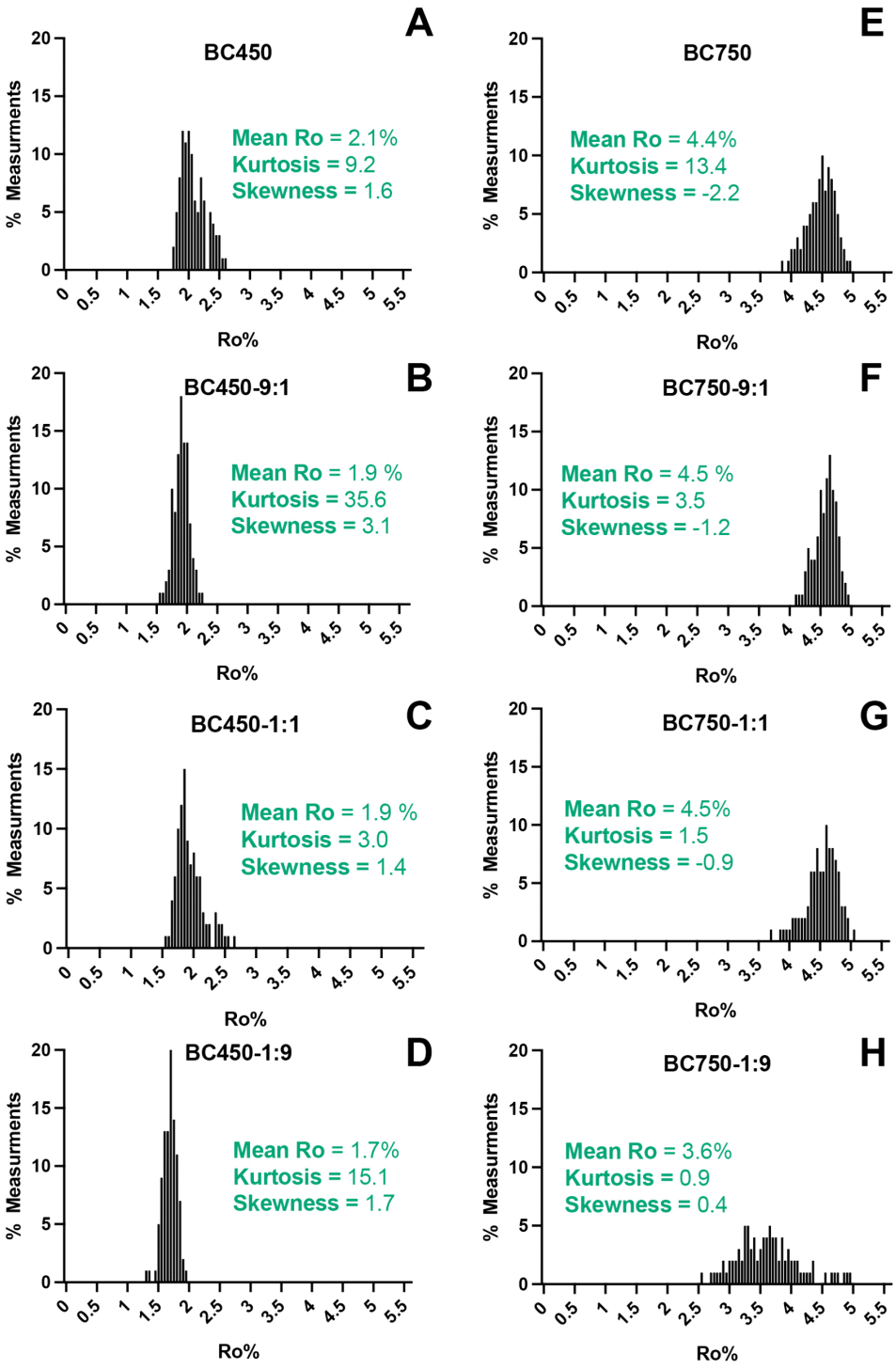

Fig 6. Histograms of random reflectance (Ro%) distributions obtained from n = 500 measurements per sample. Left column: Rock-enhanced (RE-)biochars produced at 450 °C, containing (A): 0% (BC450), (B):10% (BC450-9:1), (C): 50% (BC450-1:1) or (D): 90% basanite rock powder (BC450-1:9). Right column: RE-biochars produced at 750 °C, containing (E): 0% (BC750), (F):10% (BC750-9:1), (G): 50% (BC750-1:1) or (H): 90% basanite rock powder (BC750-1:9). Indications in green: Mean Ro%, Kurtosis (Gaussian distribution = 3, leptokurtic >3 and platykurtic <3) and Skewness (Gaussian distribution = 0, right skewed >0 and left skewed <0).

https://doi.org/10.1371/journal.pone.0355781.g006

3. Conclusions

Co-pyrolysis of biomass with silicate rock powder was proposed as an avenue to synergistically combine PyCCS- and ERW-based carbon dioxide removal in one composite material. Geogenic metals (incl. AAEM) can catalyze biomass pyrolysis and potentially engage in the formation of organo-metallic bonds (e.g., Fe-C). However, the impact of AAEM in our study is limited, as the y_c and PyC speciation (aromaticity as indicated by HyPy and BPCA-marker assessment) of RE-biochars was not altered compared to pure biochar. This suggests that up to a HTT of at least 750 °C, AAEM embedded in crystalline structures of basanite rock remain largely inactive as pyrolysis catalysts. The identification of organo-metallic bonds would require dedicated spectroscopic evidence, which was beyond the scope of this study and thus was neither confirmed nor refuted. Rock-enhancement does not impact the environmental persistence of RE-biochars – as indicated by BC_{HyPy} content and BPCA markers.

It was demonstrated that $H:C_{org}$ molar ratio of RE-biochar must be interpreted with caution. The inorganic phase can both contribute geogenic H and is able to sorb biogenic H. This is distorting the bulk $H:C_{org}$ ratio of the RE-biochar, which can no longer be interpreted independent of the inorganic phase. Also, other analytical approaches like random reflectance and thermal analysis may be compromised by matrix-effects where rock powder was added at high rates. Matrix-effects require urgent consideration during experimental design and data interpretation, not just for RE-biochar, but also for other high ash biochars. When no comparable low-ash biochar is available as a reference, as it is the case, e.g., for sewage sludge, hydrofluoric acid treatment should be tested to remove mineral components prior to elemental analysis.

Mineral surfaces exposed to syngas experience several alterations during co-pyrolysis. These include the reduction of iron-oxides, the locally discrete accumulation of K, and the pyrogenic coating with conductive secondary char. These observations provide first evidence that silicate rock particles can be modified by co-pyrolysis with biomass. These alterations may be exploited in a context of ERW (faster weathering, cf. [26]), agriculture (increased availability of nutrients, e.g., K-phosphates) and functionalized biochars (improved sorbents) – however all three fields require further research, which also needs to expand on how rock additions impact the agronomic performance of biochar.

4. Materials and methods

4.1. Biomass preparation and pyrolysis

Spruce wood shavings (*Picea abies* L.) were sourced from Allspan German Horse GmbH, Karlsruhe, Germany (50.7% C, 0.5% ash; S1 Table). Basanite rock powder ("Eifelgold"; particle size range 0–250 µm) was obtained from Provinzial-Basalt- u. Lavawerke, Sinzig, Germany and characterized by X-ray diffraction, X-ray fluorescence, laser granulometry and extraction in ultra-pure water as described elsewhere [24]. The basanite's SSA was measured as described in section 4.2. Both, pure biomass and homogenized mixtures of biomass with fine rock powder were pelleted at 6 mm without additional binders using a WK230 pellet press (Evertec, Dieburg, Germany). Afterwards, the pellets were dried (12 h at 60 °C), and fine material (< 6 mm) was removed by sieving.

The required feedstock mixing ratios to obtain RE-biochars with nominal 10%, 50% or 90% rock content, were calculated based on mass-yield (y_m) measured during production of pure biochar at 450 °C (BC450; $y_m = 25.9\%$) and at 750 °C (BC750; $y_m = 18.9\%$). The mass of the basanite was constant during pyrolysis, which was also verified by thermogravimetric analysis (TGA) of pure basanite. As some rock powder might got lost during pelleting and sieving, the actual biogenic (f_{bio}) and rock mass fraction (f_{rock}) of the feedstock was re-calculated following equation 1 and 2 (Table 3).

$$f_{rock}(\%) = Ash\ (\%) - C_{org}(\%) * r \tag{1}$$

$$f_{bio}(\%) = 100 - f_{rock}(\%) \tag{2}$$

Table 3. Composition of feedstock to produce rock-enhanced biochar (BC) at 450 °C (450) or 750 °C (750), containing 10% (9:1), 50% (1:1) or 90% (1:9) basanite rock powder after pyrolysis.

#	Sample ID	Biogenic fraction (%)	Rockfraction (%)	C_{org}(%)	Biogenic ash(%)	Total ash(%)
1	BC450	100	0	50.6	0.4	0.4
2	BC450–9:1	97.9	2.1	49.5	0.4	2.5
3	BC450–1:1	75.9	24.1	39.2	0.3	24.4
4	BC450–1:9	28.8	71.2	15.0	0.1	71.3
5	BC750	100	0	50.6	0.4	0.4
6	BC750–9:1	98.6	1.40	50.4	0.4	1.8
7	BC750–1:1	84.0	16.0	42.0	0.3	16.3
8	BC750–1:9	39.7	60.3	18.1	0.1	60.4

https://doi.org/10.1371/journal.pone.0355781.t003

With ash (%) being the ash content and C_{org} (%) the organic carbon content of the feedstock mix. The factor r describes the ratio of C_{org} to ash in the pure biomass (s1). The same procedure was applied to calculate f_{bio} and f_{rock} for RE-biochars, assuming no mass loss of rock powder during pyrolysis and no impact of rock powder on biochar dry and ash free (daf) yield.

Feedstock transport-rates (t_f in g min^{-1}) through the non-heated pyrolysis reactor were determined for each treatment by measuring material output in 10 min intervals ($n = 6$). In the same manner, biochar transport-rates (t_b in g min^{-1}) through the heated pyrolysis reactor were determined in 30 min intervals ($n = 3$). Pyrolysis was performed at 450 °C and 750 °C, respectively, with a residence time of 15 min using a PYREKA research pyrolysis unit equipped with a continuously operating auger reactor (PYREG GmbH, Dörth, Germany) under Nitrogen flow of 2 L min^{-1} [24,27]. The PYREKA operated in one continuous process per treatment.

The ratio of feedstock to biochar output during the first hour (equivalent to four reactor residence times) and after the feeder ran empty, was excluded from transport rate calculations and therefore from calculation of y_m and y_c. The biochar mass yield was calculated as follows:

$$y_m(\%) = \frac{t_b}{t_f} * 100 \tag{3}$$

With y_m being the pyrolysis mass yield as % of dry weight feedstock converted to dry weight biochar, t_f the mean transport-rate of the feedstock (g min^{-1}) and t_b the mean (RE-)biochar transport-rate (g min^{-1}). Exceptions were BC450–1:9 and BC750–1:9, here, due to the limited material volume, no transport-rate was determined but the total mass before and after pyrolysis measured. Further, the coefficient of variation (%CV) in t_b was calculated as a proxy for the variability of the continuous production process and resulting y_c.

The y_c was calculated as follows:

$$y_c(\%) = \frac{y_m * C_{org(BC)}}{C_{org(f)}} \tag{4}$$

With y_m being the mass yield of pyrolysis process (%), $C_{org(f)}$ the C_{org} content of the feedstock and $C_{org(BC)}$ the C_{org} content of the produced (RE-)biochar.

The (RE-)biochar production during the ramp-up/down time as described above was discarded not to be included in any analytical sample. The remaining production was pooled and thoroughly mixed. While many of the pellets were broken into smaller fragments by the moving parts in the reactor, ten intact pellets were randomly selected and set aside for microscopy. The remaining (RE-)biochar was milled in an impact mill with 2 mm sieve. Due to the brittle nature of the

material, a fine powder was produced this way. The particle size distribution of comparable biochars after milling was quantified by laser granulometry (Sympatec Helos KFMagic, Sympatec GmbH, Clausthal-Zellerfeld, Germany) and is typically one order of magnitude smaller than the sieve size [27] (> 90 mass-% at < 200 µm for a 2 mm sieve).

To supply larger quantities of (RE-)biochar to other follow-up experiments (not subject to this publication), a second batch of all treatments was produced. To this end, the same raw materials were used (S3 Table), pelleted by Nature Power Pellets (Wolferstadt, Germany) and pyrolyzed on the PYREKA under same process conditions as described above. The pellets produced by Nature Power Pellets had the same dimensions but a higher density. Biochar and RE-biochars from the first production batch were subject to all analytics described in section 4.2 while materials from the second batch were only subject to basic characterization (S4 Table) with additional calculation of y_m, y_c, f_{bio} and f_{rock}.

4.2 Biochar analysis

All (RE-)biochars were analyzed following the analytical guidelines of the European Biochar Certificate [78] by Eurofins Umwelt-Ost GmbH (Bobritzsch-Hilbersdorf, Germany). The C_{org} content of the daf biochar (C_{org_daf}) was calculated as follows

$$C_{org_{daf}}(\%) = \frac{C_{org}(\%)}{100\% - \mathrm{Ash}(\%)} * 100\% \quad (5)$$

With C_{org}(%) being the organic carbon content and ash (%) the total ash content of the (RE-)biochar.

The hydrogen to organic carbon molar ratio ($H{:}C_{org}$) of the bulk sample was corrected for geogenic hydrogen using equation 6.

$$H_{Bio} : C_{org} = \frac{H\%_{Bulk} - (f_{rock} * H\%_{rock})}{M_H} * \frac{M_C}{Corg\%} \quad (6)$$

With $H{:}C_{orgBio}$ being the hydrogen of the biogenic fraction to C_{org} molar ratio, i.e., the bulk ratio corrected for geogenic hydrogen, $\%H_{Bulk}$ and C_{org} content of the bulk sample, f_{rock} the rock fraction of the sample, $H\%_{rock}$ the hydrogen content of the basanite and M_C and M_H the molar mass of carbon and hydrogen. The carbon content of the rock was below the detection limit, and we assume that all rocks relevant to ERW do not contain organic carbon.

Solid state electrical conductivity (SEC) was measured using a Black Gauss I conductivity meter [79] while applying 5 t pressure (equivalent to 160 MPa) to the sample. The mineralogical composition of selected RE-biochars was measured by XRD on a D8 Advance (Bruker, Billerica USA) performed by QMineral (Heverlee, Belgium).

Thermogravimetric analysis (TGA) was conducted using an STD 650 TG-DSC system (Waters, New Castle, United States of America). Dry samples (5 mg) were heated at open, pre-weighed alumina crucibles. The temperature was then increased from 50 °C to 1000 °C at a rate of 10 °C min^{-1} under N_2 atmosphere with a flow of 50 mL min^{-1}. The recorded total weight loss was adjusted for the sample's total ash content (including rock content) to represent the weight loss of daf biochar. The fraction of biochar that remained resistant to thermal degradation up to 1000 °C is referred to as BC_{1000C}.

Benzenepolycarboxylic acids marker (BPCA) were extracted and analyzed in duplicate following Glaser *et al.* [80] and Brodowski *et al.* [81]. In brief, the (RE)-biochar samples were digested using trifluoroacetic acid to remove metal ions and organic matter including carbonates and C_{org} other than those in aromatic moieties. Then the samples were oxidized in a pressurized vessel using nitric-acid. The digests were purified from remaining polyvalent cations using exchange resins. After freeze-drying, BPCAs were trimethylsilyl derivatized and analyzed by gas chromatography connected with a flame ionization detector (GC-FID) (GC-2010 Shimadzu, Kyoto, Japan).

Two types of analytical pyrolysis were performed. Firstly, hydropyrolysis (HyPy) was performed according to Meredith *et al.* [32]. In brief, 300 mg were mixed with 10 wt% ammonium molybdate-tetrahydrate as a catalyst. The samples were

then heated in a hydrogen purged reactor under 150 bar pressure, first from ambient temperature to 250 °C at a rate of 300 °C min^{-1}, and subsequently from 250 °C to 550 °C at 8°C min^{-1}, where samples were held for 2 minutes. The residual sample was weighed and analyzed for its C_{org} content, referred to as BC_{HyPy} and presented in percent of the sample's initial C_{org}. Secondly, using a HAWK sequential-pyrolyzer with coupled TOC analyzer (Wildcat Technologies, Humble, Texas USA). Here, 10 mg were inserted into the pyrolyzer preheated to 300 °C and held for 3 min under helium atmosphere. The mass of the carbon released as CO and CO_2 was continuously measured and is referred to as S1 and relates to free hydrocarbons such as oils [76]. Then the sample was heated at 25 °C min^{-1} to 650 °C with the mass of volatilized carbon summarized as S2. After cooling to 150 °C, the atmosphere was changed to oxygen, and the sample was re-heated to 850 °C at 25 °C min^{-1} oxidizing the residual carbon [82]. S1 + S2 was defined as the reactive, labile carbon and the residual carbon was considered unreactive under the conditions applied [35,76].

Fourier transformed infrared spectroscopy was conducted using attenuated total reflectance (ATR) mode with an Invenio X FT-IR Spectrometer (Bruker Corporation, Billerica, USA). Infrared absorbance was determined from 60 consecutive scans, covering a wavenumber range of 400–4000 cm^{-1}. The absorbance spectrum was then smoothed and baseline-corrected using the software Spectragryph v.1.2.26.1.

Raman spectroscopy was conducted under a LabRAM HR 800 Raman microscope (HORIBA Europe GmbH, Oberursel, Germany), which was coupled to an BX41 light microscope (Olympus Corporation, Tokyo, Japan). All measurements used a 532 nm laser (5 mW), which scanned a 100x100 µm area. Spectral acquisition time was 10 s. Five measurements were conducted per treatment and spectra converted D/G intensity- and area ratios. The baseline correction was done using the LabSpec 6 software (Horiba) and consecutive band-fitting according to Ferrari & Robertson (2000) [83] using a Lorentzian line shape (D-band) and a Breit-Wigner-Fano line shape (G-band) with a self-made Matlab-script.

Fast field cycling ^1H nuclear magnetic resonance relaxometry (^1H FFC-NMR, i.e., ^1H Relaxometry) was performed following Conte (2021) [59]. Briefly, samples of 1 g sample was weighed in a 10 mm NMR tubes, then water was added in 2.5:1 ratio. The mixture was vortexed for 5 minutes and left to settle for 24 h. Measurements were conducted on a Stelar Smartracer Fast-Field-Cycling Relaxometer (Stelar SRL, Mede, Italy) set to 25 °C. The proton spins were polarized at a polarization field (B_{POL}) corresponding to a proton Larmor frequency (n_L) of 10 MHz for a period (T_{POL}) of about five times the T_1 estimated at this frequency. After each B_{POL}, the magnetic field intensity (B_{RLX}) was set at the proton Larmor frequency, n_L, of 1 MHz. The period τ, during which B_{RLX} was applied, has been varied on 32 logarithmic spaced time sets. Free induction decays (FID) at each τ value were recorded following a single ^1H 90 ° pulse applied at an acquisition field (B_{ACQ}) corresponding to n_L of 7.2 MHz. A time domain of 100 µs sampled with 512 points was applied. Field-switching time was 3 ms, while spectrometer dead time was 15 µs. For all the experiments, a recycle delay of 2 s was used. All decay curves acquired were analyzed by the UPEN algorithm to obtain the relaxograms [84,85]. Relaxograms were finally used to calculate the Pore Connectivity Index (PCI) [86] (additional S12 Text).

For SEM, RE-biochar pellets were mounted on an aluminum sample holder using carbon pads (Plano GmbH, Wetzlar, Germany) and sputter-coating them with gold (3–5 nm) using a Cressington 108auto (TESCAN GmbH, Dortmund, Germany). Analysis was conducted with a JSM-6610 LV (JEOL Ltd., Tokyo, Japan) at a working distance of 11 mm and acceleration voltage of 15 kV. Backscattered electron images (BES) were acquired, and Energy-dispersive X-ray (EDX) analysis of the same clippings was carried out using a 20 mm^2 Oxford X-max detector (Oxford Instruments, Abingdon, United Kingdom).

For Scanning Transmission Electron Microscopy (STEM) with Electron Energy Loss Spectroscopy (EELS) specimens, Re-biochar samples (< 3 mm), were embedded in epoxy resin (Spezifix 40, Struers, Willich, Germany). Ultrathin sections of 50 nm were prepared using a Leica EM UC6-NT ultramicrotome (Leica Microsystems, Vienna, Austria) equipped with a 35° ultra diamond knife (Diatome, Biel, Switzerland). The sections were transferred onto lacey carbon-coated copper grids using a Perfect Loop (Diatome). The measurements were performed using a monochromated probe corrected FEI Titan G2 60–300 STEM-microscope with a Schottky-type X-FEG electron source operated at 300 kV. The microscope

was equipped with a Gatan Imaging Filter, Quantum including a direct electron detection camera (K2 Summit) and a CCD camera (Ultrascan1000) with dual-EELS capability. The microscope was operated in monochromated mode with a semi-convergence angle of 15.6 mrad and a beam current of about 200 pA, resulting in a spatial resolution of 0.12 nm and an energy resolution at full-width at half maximum of 0.3 eV. The measurements were performed at a temperature of −160 °C using a cryo TEM-holder (Mel-Build, Fukuoka, Japan). The high angular annual dark field (HAADF) detector was used for micrographs acquisition.

Gas adsorption was performed using nitrogen isotherms at 77 K on an AUTOSORB-IQ volumetric sorption device (3P-Instruments GmbH & Co KG, Odelzhausen, Germany). Samples of 0.1-0.2 g biochar were degassed at 150 °C for 12 h with a final vacuum of $<10^{-2}$ Pa applied before analysis. Surface area (Brunauer-Emmett-Teller method) was calculated following the guidelines of DIN ISO 9277:2014. The pore volume distribution is inferred from the total pore volume determined at $P/P_0 = 0.99$ (Gurvich's law) and measured adsorption isotherms according to the density functional theory (DFT) [87].

The magnetic susceptibility was measured on $6.4x10^{-6}$ m^3 cubes of manually compressed material. Measurements were conducted in a 200 A m^{-1} field at low (976 Hz) and high (15616 Hz) frequency (χlf and χhf) using a MFK1-FA Kappabridge (AGICO Inc., Brno, Czech Republic). The frequency dependent magnetic susceptibility was calculated as [(χlf—χhf)/χlf] × 100 [57,60].

Random Reflectance (Ro%) was measured on (RE)-biochar fragments between 63 and 1000 μm, that were embedded in an epoxy-resin and polished (ISO 7404−2 2009). White light reflectance measurements (ISO 7404−5, 2009) were carried out using a Zeiss Axio Imager II microscope (Zeiss, Oberkochen, Germany) with integrated Discus-Fossil system (Hilgers Technisches Buero, Königswinter, Germany). Measurements were conducted manually on $n = 500$ randomly selected, exposed macerals, with each measurement covering an area of 0.3 μm². Reflectance measurements were calibrated using KB N Lasf1.317 and KB cubic zirconia 3.11 standards.

4.3. Statistical considerations

Rock-enhanced biochars were produced in a single continuous batch, with RE-biochar yield recorded at regular intervals and the coefficient of variation of f_b and y_c calculated. In general, analyses were conducted on representative samples without replication ($n = 1$). Depending on the analytical method varying numbers of repeated measures were conducted per sample (e.g., Raman spectroscopy with $n = 5$, FTIR with $n = 60$, and random reflectance with $n = 500$). Mean, median, skewness and kurtosis of each Ro distribution were calculated using Microsoft Excel.

Supporting information

S1 Table. Biomass analysis.
(PDF)

S2 Table. Rock characterization.
(PDF)

S3 Table. Feedstock composition (2nd batch).
(PDF)

S4 Table. Biochar basic characterization (2nd batch).
(PDF)

S5 Fig. ATR-FTIR absorbance spectra.
(PDF)

S6 Fig. Raman spectra (D/G ratios).
(PDF)

S7 Fig. Graphical Abstract.
(TIF)

S7 Table. Biochar main and trace elements (1st batch).
(PDF)

S8 Table. Hydrogen in small hydrocarbons.
(PDF)

S9 Fig. Specific surface area and pore volume distribution.
(PDF)

S10 Fig. STEM-EELS transects with inverted beam trajectory.
(PDF)

S11 Fig. SEM/EDX potassium distribution mapping.
(PDF)

S12 Text. Methods – Pore Connectivity Index.
(PDF)

Acknowledgments

We appreciate the support in material characterization by Eurofins Umwelt Ost GmbH laboratories (Bobritzsch-Hilbersdorf, Germany), QMinerals (Leuven, Belgium) and the Institute of Process Engineering at Offenburg University of Applied Sciences (Offenburg, Germany).

Author contributions

Conceptualization: Johannes Meyer zu Drewer, Hans-Peter Schmidt, Nikolas Hagemann.

Formal analysis: Johannes Meyer zu Drewer.

Funding acquisition: Nikolas Hagemann.

Investigation: Johannes Meyer zu Drewer, Tobias Bromm, José María de la Rosa, Harald Fitzek, Amin Ghafarpour, Calogero Librici, Jens Möllmer, Michael Oberaigner, Sara Maria Pérez-Dalí, Arka Rudra, Águeda Sánchez-Martín, Hamed Sanei.

Methodology: Johannes Meyer zu Drewer, Nikolas Hagemann.

Resources: Thomas D. Bucheli, Pellegrino Conte, José María de la Rosa, Bruno Glaser, Andreas Kappler, Jens Möllmer, Hamed Sanei.

Visualization: Johannes Meyer zu Drewer, Michael Oberaigner.

Writing – original draft: Johannes Meyer zu Drewer.

Writing – review & editing: Tobias Bromm, Thomas D. Bucheli, Pellegrino Conte, José María de la Rosa, Harald Fitzek, Amin Ghafarpour, Bruno Glaser, Andreas Kappler, Calogero Librici, Jens Möllmer, Michael Oberaigner, Sara Maria Pérez-Dalí, Arka Rudra, Águeda Sánchez-Martín, Hamed Sanei, Hans-Peter Schmidt, Nikolas Hagemann.

References

1. Rawal A, Joseph SD, Hook JM, Chia CH, Munroe PR, Donne S, et al. Mineral-Biochar Composites: Molecular Structure and Porosity. Environ Sci Technol. 2016;50(14):7706–14. https://doi.org/10.1021/acs.est.6b00685 PMID: 27284608

2. Joseph S, Graber E, Chia C, Munroe P, Donne S, Thomas T, et al. Shifting paradigms: development of high-efficiency biochar fertilizers based on nano-structures and soluble components. Carbon Management. 2013;4(3):323–43. https://doi.org/10.4155/cmt.13.23
3. Nan H, Yang F, Zhao L, Mašek O, Cao X, Xiao Z. Interaction of Inherent Minerals with Carbon during Biomass Pyrolysis Weakens Biochar Carbon Sequestration Potential. ACS Sustainable Chem Eng. 2018;7(1):1591–9. https://doi.org/10.1021/acssuschemeng.8b05364
4. Buss W, Jansson S, Wurzer C, Mašek O. Synergies between BECCS and Biochar—Maximizing Carbon Sequestration Potential by Recycling Wood Ash. ACS Sustainable Chem Eng. 2019;7(4):4204–9. https://doi.org/10.1021/acssuschemeng.8b05871
5. Mašek O, Buss W, Brownsort P, Rovere M, Tagliaferro A, Zhao L, et al. Potassium doping increases biochar carbon sequestration potential by 45%, facilitating decoupling of carbon sequestration from soil improvement. Sci Rep. 2019;9(1):5514. https://doi.org/10.1038/s41598-019-41953-0 PMID: 30940871
6. Grafmüller J, Böhm A, Zhuang Y, Spahr S, Müller P, Otto TN, et al. Wood Ash as an Additive in Biomass Pyrolysis: Effects on Biochar Yield, Properties, and Agricultural Performance. ACS Sustainable Chem Eng. 2022;10(8):2720–9. https://doi.org/10.1021/acssuschemeng.1c07694
7. Buss W, Bogush A, Ignatyev K, Mašek O. Unlocking the Fertilizer Potential of Waste-Derived Biochar. ACS Sustainable Chem Eng. 2020;8(32):12295–303. https://doi.org/10.1021/acssuschemeng.0c04336
8. Zhao Z, Nie T, Zhou W. Enhanced biochar stabilities and adsorption properties for tetracycline by synthesizing silica-composited biochar. Environ Pollut. 2019;254(Pt A):113015. https://doi.org/10.1016/j.envpol.2019.113015 PMID: 31400663
9. Gitipour S, Sanaei M, Lak R, Karbassi A. Effective elimination of Pb (II) cations from waste water and polluted water using siderite magnetic biochar. Sci Rep. 2025;15(1):7912. https://doi.org/10.1038/s41598-025-92073-x PMID: 40050328
10. Zhang L, Dong Y, Liu J, Liu C, Liu W, Lin H. The effect of co-pyrolysis temperature for iron-biochar composites on their adsorption behavior of antimonite and antimonate in aqueous solution. Bioresour Technol. 2022;347:126362. https://doi.org/10.1016/j.biortech.2021.126362 PMID: 34838625
11. Giudicianni P, Gargiulo V, Grottola CM, Alfè M, Ferreiro AI, Mendes MAA. Inherent metal elements in biomass pyrolysis: a review. Energy Fuels. 2021;35:5407–78. https://doi.org/10.1021/acs.energyfuels.0c04046
12. Buss W, Wurzer C, Manning DAC, Rohling EJ, Borevitz J, Mašek O. Mineral-enriched biochar delivers enhanced nutrient recovery and carbon dioxide removal. Commun Earth Environ. 2022;3(1). https://doi.org/10.1038/s43247-022-00394-w
13. Yang F, Gao P, Chi L, Gao Z, Wang Y, Luo L, et al. Enhancement of Biochar Carbon Sequestration Through Mineral Regulation: Effects and Mechanisms. Agronomy. 2025;15:943. https://doi.org/10.3390/agronomy15040943
14. Nan H, Mašek O, Yang F, Xu X, Qiu H, Cao X, et al. Minerals: A missing role for enhanced biochar carbon sequestration from the thermal conversion of biomass to the application in soil. Earth-Science Reviews. 2022;234:104215. https://doi.org/10.1016/j.earscirev.2022.104215
15. Guo J, Chen B. Insights on the molecular mechanism for the recalcitrance of biochars: interactive effects of carbon and silicon components. Environ Sci Technol. 2014;48(16):9103–12. https://doi.org/10.1021/es405647e PMID: 25017808
16. Nan H, Zhao L, Yang F, Liu Y, Xiao Z, Cao X, et al. Different alkaline minerals interacted with biomass carbon during pyrolysis: Which one improved biochar carbon sequestration? Journal of Cleaner Production. 2020;255:120162. https://doi.org/10.1016/j.jclepro.2020.120162
17. Hartmann J, West AJ, Renforth P, Köhler P, De La Rocha CL, Wolf-Gladrow DA, et al. Enhanced chemical weathering as a geoengineering strategy to reduce atmospheric carbon dioxide, supply nutrients, and mitigate ocean acidification. Reviews of Geophysics. 2013;51(2):113–49. https://doi.org/10.1002/rog.20004
18. Beerling DJ, Kantzas EP, Lomas MR, Wade P, Eufrasio RM, Renforth P, et al. Potential for large-scale CO2 removal via enhanced rock weathering with croplands. Nature. 2020;583(7815):242–8. https://doi.org/10.1038/s41586-020-2448-9 PMID: 32641817
19. Schiedung M, Harrington KJ, Dupla X, Möller B, Facq E, Sweere T, et al. Uncertainties of enhanced rock weathering for climate-change mitigation. Nat Rev Earth Environ. 2026;7(4):253–66. https://doi.org/10.1038/s43017-026-00761-7
20. Swoboda P, Döring TF, Hamer M. Remineralizing soils? The agricultural usage of silicate rock powders: A review. Sci Total Environ. 2022;807(Pt 3):150976. https://doi.org/10.1016/j.scitotenv.2021.150976 PMID: 34662609
21. Te Pas EEEM, Hagens M, Comans RNJ. Assessment of the enhanced weathering potential of different silicate minerals to improve soil quality and sequester CO2. Front Clim. 2023;4:954064. https://doi.org/10.3389/fclim.2022.954064
22. Beerling DJ, Epihov DZ, Kantola IB, Masters MD, Reershemius T, Planavsky NJ, et al. Enhanced weathering in the US Corn Belt delivers carbon removal with agronomic benefits. Proc Natl Acad Sci U S A. 2024;121(9):e2319436121. https://doi.org/10.1073/pnas.2319436121 PMID: 38386712
23. Buss W, Hasemer H, Sokol NW, Rohling EJ, Borevitz J. Applying minerals to soil to draw down atmospheric carbon dioxide through synergistic organic and inorganic pathways. Commun Earth Environ. 2024;5(1). https://doi.org/10.1038/s43247-024-01771-3
24. Meyer zu Drewer J, Vorrath M-E, Amann T, Hartmann J, De la Rosa JM, Möllmer J, et al. Pyrogenic carbon and carbonating minerals for carbon capture and storage (PyMiCCS) part I: production, physico-chemical characterization and C-sink potential. Front Clim. 2025;7. https://doi.org/10.3389/fclim.2025.1631368
25. Vorrath M-E, Amann T, Meyer zu Drewer J, Hagemann N, Aldrich C, Börker J. Pyrogenic carbon and carbonating minerals for carbon capture and storage (PyMiCCS) part II: organic and inorganic carbon dioxide removal in an Oxisol. Frontiers in Climate. 2025;7. https://doi.org/10.3389/fclim.2025.1592454
26. Meyer zu Drewer J, Vorrath M-E, Amann T, Hartmann J, Ansari M, Cárcamo Pérez M, et al. Combining biochar and basanite rock powder enhances carbon dioxide removal by carbonate alkalinity production. Front Clim. 2026;8. https://doi.org/10.3389/fclim.2026.1853116

27. Hagemann N, Schmidt H-P, Kägi R, Böhler M, Sigmund G, Maccagnan A, et al. Wood-based activated biochar to eliminate organic micropollutants from biologically treated wastewater. Sci Total Environ. 2020;730:138417. https://doi.org/10.1016/j.scitotenv.2020.138417 PMID: 32388360
28. Schmidt H, Anca-Couce A, Hagemann N, Werner C, Gerten D, Lucht W, et al. Pyrogenic carbon capture and storage. GCB Bioenergy. 2018;11(4):573–91. https://doi.org/10.1111/gcbb.12553
29. Ippolito JA, Cui L, Kammann C, Wrage-Mönnig N, Estavillo JM, Fuertes-Mendizabal T, et al. Feedstock choice, pyrolysis temperature and type influence biochar characteristics: a comprehensive meta-data analysis review. Biochar. 2020;2(4):421–38. https://doi.org/10.1007/s42773-020-00067-x
30. Lebrun Thauront J, Soja G, Schmidt H-P, Abiven S. A critical re-analysis of biochar properties prediction from production parameters and elemental analysis. GCB Bioenergy. 2024;16:e13170. doi:https://doi.org/10.1111/gcbb.13170
31. Glaser B, Guenther M, Maennicke H, Bromm T. Microwave-assisted combustion to produce benzene polycarboxylic acids as molecular markers for biochar identification and quantification. Biochar. 2021;3(4):407–18. https://doi.org/10.1007/s42773-021-00124-z
32. Meredith W, McBeath AV, Ascough P, Bird M. Analysis of biochars by hydropyrolysis. In: Singh B, Camps-Arbestain M, Lehmann J, editors. Biochar: A Guide to Analytical Methods. Csiro Publishing. 2017:320.
33. Hagemann N, Schmidt H-P, Bucheli TD, Grafmüller J, Vosswinkel S, Herdegen V, et al. Proxies for use in biochar decay models: Hydropyrolysis, electric conductivity, and H/Corg molar ratio. PLoS One. 2025;20(9):e0330206. https://doi.org/10.1371/journal.pone.0330206 PMID: 40892728
34. Zhang J, Wang J, Wu Z, Wang S, Wu Y, Liu X. Heteroatom (nitrogen/sulfur)-doped graphene as an efficient electrocatalyst for oxygen reduction and evolution reactions. Catalysts. 2018;8:475. https://doi.org/10.3390/catal8100475
35. Sanei H, Rudra A, Przyswitt ZMM, Kousted S, Sindlev MB, Zheng X, et al. Assessing biochar's permanence: An inertinite benchmark. International Journal of Coal Geology. 2024;281:104409. https://doi.org/10.1016/j.coal.2023.104409
36. Anca-Couce A, Mehrabian R, Scharler R, Obernberger I. Kinetic scheme of biomass pyrolysis considering secondary charring reactions. Energ Convers Manage. 2014;87:687–96. https://doi.org/10.1016/j.enconman.2014.07.061
37. Johansson KO, Head-Gordon MP, Schrader PE, Wilson KR, Michelsen HA. Resonance-stabilized hydrocarbon-radical chain reactions may explain soot inception and growth. Science. 2018;361(6406):997–1000. https://doi.org/10.1126/science.aat3417 PMID: 30190399
38. Gustafsson Ö, Bucheli TD, Kukulska Z, Andersson M, Largeau C, Rouzaud J, et al. Evaluation of a protocol for the quantification of black carbon in sediments. Global Biogeochemical Cycles. 2001;15(4):881–90. https://doi.org/10.1029/2000gb001380
39. Feng D, Guo D, Shang Q, Zhao Y, Zhang L, Guo X, et al. Mechanism of biochar-gas-tar-soot formation during pyrolysis of different biomass feedstocks: Effect of inherent metal species. Fuel. 2021;293:120409. https://doi.org/10.1016/j.fuel.2021.120409
40. Buchanan AC, Britt PF. Investigations of restricted mass transport effects on hydrocarbon pyrolysis mechanisms through silica immobilization. J Anal Appl Pyrol. 2000;54:127–51. https://doi.org/10.1016/S0165-2370(99)00078-9
41. Lopez G, Santamaria L, Lemonidou A, Zhang S, Wu C, Sipra AT, et al. Hydrogen generation from biomass by pyrolysis. Nat Rev Methods Primers. 2022;2(1). https://doi.org/10.1038/s43586-022-00097-8
42. Glushkov DO, Nyashina GS, Anand R, Strizhak PA. Composition of gas produced from the direct combustion and pyrolysis of biomass. Process Safety and Environmental Protection. 2021;156:43–56. https://doi.org/10.1016/j.psep.2021.09.039
43. Zhang Y, Liang Y, Li S, Yuan Y, Zhang D, Wu Y, et al. A review of biomass pyrolysis gas: Forming mechanisms, influencing parameters, and product application upgrades. Fuel. 2023;347:128461. https://doi.org/10.1016/j.fuel.2023.128461
44. Demirbas A, Arin G. Hydrogen from Biomass via Pyrolysis: Relationships between Yield of Hydrogen and Temperature. Energy Sources. 2004;26(11):1061–9. https://doi.org/10.1080/00908310490494568
45. Uddin MdN, Daud WMAW, Abbas HF. Effects of pyrolysis parameters on hydrogen formations from biomass: a review. RSC Adv. 2014;4(21):10467. https://doi.org/10.1039/c3ra43972k
46. Wang L, Jin Z, Huang X, Liu R, Su Y, Zhang Q. Hydrogen Adsorption in Porous Geological Materials: A Review. Sustainability. 2024;16:1958. https://doi.org/10.3390/su16051958
47. Wang L, Cheng J, Jin Z, Sun Q, Zou R, Meng Q, et al. High-pressure hydrogen adsorption in clay minerals: Insights on natural hydrogen exploration. Fuel. 2023;344:127919. https://doi.org/10.1016/j.fuel.2023.127919
48. Ziemiański PP, Derkowski A. Structural and textural control of high-pressure hydrogen adsorption on expandable and non-expandable clay minerals in geologic conditions. International Journal of Hydrogen Energy. 2022;47(67):28794–805. https://doi.org/10.1016/j.ijhydene.2022.06.204
49. Prins R. Hydrogen Spillover. Facts and Fiction. Chem Rev. 2012;112:2714–38. https://doi.org/10.1021/cr200346z
50. Smyth JR, Frost DJ, Nestola F, Holl CM, Bromiley G. Olivine hydration in the deep upper mantle: Effects of temperature and silica activity. Geophysical Research Letters. 2006;33(15). https://doi.org/10.1029/2006gl026194
51. Fei H, Katsura T. Pressure Dependence of Proton Incorporation and Water Solubility in Olivine. JGR Solid Earth. 2020;125(2). https://doi.org/10.1029/2019jb018813
52. Sundvall R, Skogby H. Hydrogen defect saturation in natural pyroxene. Phys Chem Minerals. 2011;38(5):335–44. https://doi.org/10.1007/s00269-010-0407-y
53. Wei R, Cang D, Bai Y, Huang D, Liu X. Reduction characteristics and kinetics of iron oxide by carbon in biomass. Ironmaking & Steelmaking. 2016;43(2):144–52. https://doi.org/10.1179/1743281215y.0000000061

54. Bagatini MC, Kan T, Evans TJ, Strezov V. Iron Ore Reduction by Biomass Volatiles. J Sustain Metall. 2021;7:215–26. https://doi.org/10.1007/s40831-021-00337-3
55. Deng J, Ning X-A, Shen J, Ou W, Chen J, Qiu G, et al. Biomass waste as a clean reductant for iron recovery of iron tailings by magnetization roasting. J Environ Manage. 2022;317:115435. https://doi.org/10.1016/j.jenvman.2022.115435 PMID: 35751253
56. Qiu G, Ning X, Shen J, Wang Y, Zhang D, Deng J. Recovery of iron from iron tailings by suspension magnetization roasting with biomass-derived pyrolytic gas. Waste Manag. 2023;156:255–63. https://doi.org/10.1016/j.wasman.2022.11.034 PMID: 36508909
57. Ghafarpour A, Khormali F, Tazikeh H, Kehl M, Rolf C, Frechen M. Geophysical sediment properties of a late Pleistocene loess–paleosol sequence, Chenarli, northeastern Iran. Quat Res. 2023;114:114–29. https://doi.org/10.1017/qua.2023.5
58. Wang S, Zhao M, Zhou M, Zhao Y, Li YC, Gao B, et al. Biomass facilitated phase transformation of natural hematite at high temperatures and sorption of Cd2+ and Cu2. Environ Int. 2019;124:473–81. https://doi.org/10.1016/j.envint.2019.01.004 PMID: 30684805
59. Conte P. Applications of fast field cycling NMR relaxometry. Annual Reports on NMR Spectroscopy. 2021;141–88. https://doi.org/10.1016/bs.arnmr.2021.05.001
60. Dearing JA, Hay KL, Baban SMJ, Huddleston AS, Wellington EMH, Loveland PJ. Magnetic susceptibility of soil: an evaluation of conflicting theories using a national data set. Geophysical Journal International. 1996;127(3):728–34. https://doi.org/10.1111/j.1365-246x.1996.tb04051.x
61. Webber JBW, Corbett P, Semple KT, Ogbonnaya U, Teel WS, Masiello CA, et al. An NMR study of porous rock and biochar containing organic material. Microporous and Mesoporous Materials. 2013;178:94–8. https://doi.org/10.1016/j.micromeso.2013.04.004
62. Morjan I, Alexandrescu R, Scarisoreanu M, Fleaca C, Dumitrache F, Soare I, et al. Controlled manufacturing of nanoparticles by the laser pyrolysis: Application to cementite iron carbide. Applied Surface Science. 2009;255(24):9638–42. https://doi.org/10.1016/j.apsusc.2009.04.125
63. Hagemann N, Joseph S, Schmidt H-P, Kammann CI, Harter J, Borch T, et al. Organic coating on biochar explains its nutrient retention and stimulation of soil fertility. Nat Commun. 2017;8(1):1089. https://doi.org/10.1038/s41467-017-01123-0 PMID: 29057875
64. Muller DA, Sorsch T, Moccio S, Baumann FH, Evans-Lutterodt K, Timp G. The electronic structure at the atomic scale of ultrathin gate oxides. Nature. 1999;399(6738):758–61. https://doi.org/10.1038/21602
65. Kleber M, Nico PS, Plante A, Filley T, Kramer M, Swanston C, et al. Old and stable soil organic matter is not necessarily chemically recalcitrant: implications for modeling concepts and temperature sensitivity. Global Change Biology. 2011;17(2):1097–107. https://doi.org/10.1111/j.1365-2486.2010.02278.x
66. Pal R, Bourgeois L, Weyland M, Sikder AK, Saito K, Funston AM, et al. Chemical Fingerprinting of Polymers Using Electron Energy-Loss Spectroscopy. ACS Omega. 2021;6(37):23934–42. https://doi.org/10.1021/acsomega.1c02939 PMID: 34568672
67. Cody GD, Gupta NS, Briggs DEG, Kilcoyne ALD, Summons RE, Kenig F, et al. Molecular signature of chitin-protein complex in Paleozoic arthropods. Geology. 2011;39(3):255–8. https://doi.org/10.1130/g31648.1
68. Espitalié J, Senga Makadi K, Trichet J. Role of the mineral matrix during kerogen pyrolysis. Organic Geochemistry. 1984;6:365–82. https://doi.org/10.1016/0146-6380(84)90059-7
69. Bährle C, Custodis V, Jeschke G, van Bokhoven JA, Vogel F. The Influence of Zeolites on Radical Formation During Lignin Pyrolysis. ChemSusChem. 2016;9(17):2397–403. https://doi.org/10.1002/cssc.201600582 PMID: 27486717
70. Suzuki S, Bower C, Zhou O. In-situ TEM and EELS studies of alkali–metal intercalation with single-walled carbon nanotubes. Chemical Physics Letters. 1998;285(3–4):230–4. https://doi.org/10.1016/s0009-2614(98)00051-7
71. Jiang N, Spence JCH. Interpretation of Oxygen K pre-edge peak in complex oxides. Ultramicroscopy. 2006;106(3):215–9. https://doi.org/10.1016/j.ultramic.2005.07.004 PMID: 16125324
72. Bi D, Yin M, Huang F, Zhang J, Yi W. Evolution and prediction model of environmentally-persistent free radicals in biomass three-component pyrolytic carbon with pyrolysis temperature. Industrial Crops and Products. 2023;206:117643. https://doi.org/10.1016/j.indcrop.2023.117643
73. Ma L, Syed-Hassan SSA, Zhou J, Deng W, Xiong Y, Wang X, et al. Effect of alkali and alkali earth metals on reactions of stable free radicals during biomass pyrolysis: An in-situ EPR study. Fuel Processing Technology. 2023;250:107916. https://doi.org/10.1016/j.fuproc.2023.107916
74. Wang T, Camps-Arbestain M, Hedley M. Predicting C aromaticity of biochars based on their elemental composition. Organic Geochemistry. 2013;62:1–6. https://doi.org/10.1016/j.orggeochem.2013.06.012
75. Mastalerz M, Drobniak A, Liu B, Sauer PE. Reflectance as an indicator of biochar permanence. International Journal of Coal Geology. 2025;306:104809. https://doi.org/10.1016/j.coal.2025.104809
76. Rudra A, Petersen HI, Sanei H. Molecular characterization of biochar and the relation to carbon permanence. International Journal of Coal Geology. 2024;291:104565. https://doi.org/10.1016/j.coal.2024.104565
77. Sanei H, Wojtaszek-Kalaitzidi M, Schovsbo NH, Stenshøj R, Zhou Z, Schmidt H-P, et al. Quantifying inertinite carbon in biochar. International Journal of Coal Geology. 2025;310:104886. https://doi.org/10.1016/j.coal.2025.104886
78. EBC. European Biochar Certificate – Guidelines for a Sustainable Production of Biochar. Frick, Switzerland: Carbon Standards International. 2025. http://carbon-standards.com/ebc
79. Eurofins-Umwelt-Ost-GmbH. Conductivity meter Black Gauss I - technical documentation. 2023. doi:https://doi.org/10.5281/zenodo.8197758
80. Glaser B, Haumaier L, Guggenberger G, Zech W. Black carbon in soils: the use of benzenecarboxylic acids as specific markers. Organic Geochemistry. 1998;29(4):811–9. https://doi.org/10.1016/s0146-6380(98)00194-6

81. Brodowski S, Rodionov A, Haumaier L, Glaser B, Amelung W. Revised black carbon assessment using benzene polycarboxylic acids. Organic Geochemistry. 2005;36(9):1299–310. https://doi.org/10.1016/j.orggeochem.2005.03.011

82. Lafargue E, Marquis F, Pillot D. Rock-Eval 6 Applications in Hydrocarbon Exploration, Production, and Soil Contamination Studies. Rev Inst Fr Pét. 1998;53:421–37. https://doi.org/10.2516/ogst:1998036

83. Ferrari AC, Robertson J. Interpretation of Raman spectra of disordered and amorphous carbon. Phys Rev B. 2000;61:14095–107. https://doi.org/10.1103/PhysRevB.61.14095

84. Bortolotti V, Brown RJS, Fantazzini P, Landi G, Zama F. Uniform Penalty inversion of two-dimensional NMR relaxation data. Inverse Problems. 2016;33(1):015003. https://doi.org/10.1088/1361-6420/33/1/015003

85. Bortolotti V, Brown RJS, Fantazzini P, Landi G, Zama F. I2DUPEN: Improved 2DUPEN algorithm for inversion of two-dimensional NMR data. Microporous and Mesoporous Materials. 2018;269:195–8. https://doi.org/10.1016/j.micromeso.2017.04.038

86. Lo Meo P, Mundo F, Terranova S, Conte P, Chillura Martino D. Water Dynamics at the Solid-Liquid Interface to Unveil the Textural Features of Synthetic Nanosponges. J Phys Chem B. 2020;124(9):1847–57. https://doi.org/10.1021/acs.jpcb.9b11935 PMID: 32069049

87. Lowell S, Shields JE, Thomas MA, Thommes M. Characterization of Porous Solids and Powders: Surface Area, Pore Size and Density. Dordrecht: Springer. 2004.